

STELLAR X-RAY ACTIVITY ACROSS THE HERTZSPRUNG-RUSSELL DIAGRAM. I. CATALOGS

SONG WANG¹, YU BAI¹, LIN HE², JIFENG LIU^{1,3,4}

Draft version September 8, 2020

ABSTRACT

Stellar magnetic activity provides substantial information on the magnetic dynamo and the coronal heating process. We present a catalog of X-ray activity for about 6000 stars, based on the *Chandra* and *Gaia* DR2 data. We also classified more than 3000 stars as young stellar objects, dwarf stars, or giant stars. By using the stars with valid stellar parameters and classifications, we studied the distribution of X-ray luminosity (L_X) and the ratio of X-ray-to-bolometric luminosities (R_X), the positive relation between L_X , R_X , and hardness ratio, and the long-term X-ray variation. This catalog can be used to investigate some important scientific topics, including the activity-rotation relation, the comparison between different activity indicators, and the activities of interesting objects (e.g., A-type stars and giants). As an example, we use the catalog to study the activity-rotation relation, and find that the young stellar objects, dwarfs, and giants fall on a single sequence in the relation R_X versus Rossby number, while the giants do not follow the relation R_X versus $P_{\text{rot}}^{-2}R^{-4}$ valid for dwarfs.

Keywords: X-rays: stars – stars: activity – stars: late-type

1. INTRODUCTION

The detailed physical process responsible for coronal heating remains one major open problem in astrophysics (Rosner 1980; Parker 1988; Hudson 1991; Klimchuk 2006; van Ballegoijen et al. 2011). The most popular heating mechanisms include dissipation of magnetic stresses as in the “nanoflare” model with the twisting of magnetic field lines and subsequent magnetic reconnection (e.g., Parker 1988; Priest et al. 2002), and dissipation of magnetohydrodynamic (Alfvén) waves (e.g., van Ballegoijen et al. 2011, 2014). Studies of stellar magnetic activity can help advance our understanding of the characteristics of magnetic field, and of the process that heats the outer atmosphere (Testa et al. 2015).

One key question about the magnetic activity is the magnetic dynamo in different type stars. In the solar-type dynamo mechanism (α - Ω dynamo or tachocline dynamo), the magnetic field is generated in the deep convection zones because of the interior radial differential rotation and amplified by the interaction between magnetic flux tubes and the convection; the magnetic field then rises to the stellar surface and produce chromospheric heating through interaction with the uppermost convection zones (e.g., Parker 1975; Reid & Hawley 2000). Fully convective stars (e.g., T Tauri stars, very late M dwarfs) do not have a tachocline and their dynamo mechanism is expected to be very different. However, there is no precipitate decline or change in coronal properties between fully convective stars and stars with tachoclines (Testa et al. 2015). Some studies even found that fully convective stars also operate a solar-type dynamo (e.g., Wright & Drake 2016). It therefore suggests that the

tachocline is not vital in the generation of the magnetic field and the dynamo may originate throughout the convection zone (Wright & Drake 2016).

The magnetic dynamo can be observationally tested from stellar activities in different parts of stellar atmospheres, such as star spots, flares, and X-ray emission. Stellar activity is ubiquitous in late-type stars, and strongly depends on stellar parameters (e.g., stellar mass, age, metallicity). Significant progress have been made in recent years, including the activity-rotation relationship (Pizzolato et al. 2003; Wright et al. 2011), the evolution of activity with stellar age (Mamaĵek & Hillenbrand 2008; Pace 2013; van Saders & Pinsonneault 2013; Reinhold & Gizon 2015), the Gyrochronology (Barnes 2003, 2007, 2010; McQuillan et al. 2014; Meibom et al. 2015), flaring activity (Shibayama et al. 2013; Hawley et al. 2014; Balona 2015; Yang & Liu 2019), and stellar cycles (Mathur et al. 2014; Ferreira Lopes et al. 2015). On the other hand, the growing number of observations and data raise new questions about stellar magnetic activity. Giants, which are expected to harbor weak surface magnetic fields due to slow rotation, show clear activities (Aurière et al. 2015; He et al. 2019); A-type stars, with shallow convective envelopes, also show substantial activities (Balona 2012, 2013, 2017). However, some studies argued that these stars belong to binary systems and the activities are attributed to their unresolved low-mass companions (e.g., Pedersen et al. 2017; Özdarcın & Dal 2018).

These advances in observations and theory can also help us explore the solar-stellar connection (e.g., Rosner et al. 1985; Peres et al. 1997, 2000; Brun et al. 2015). Although the solar and stellar activity show close similarity, many differences have been observed. Active stars tend to have large polar spots (e.g., Berdyugina et al. 1998; Hussain et al. 2007), quite unlike the sun. A typical flare on the sun lasts several minutes with energy ranging from 10^{29} to 10^{32} erg, which can be well supported by the classical model

¹ Key Laboratory of Optical Astronomy, National Astronomical Observatories, Chinese Academy of Sciences, Beijing 100101, China; songw@bao.ac.cn

² Hebei University of Science and Technology, Shijiazhuang 050018, China

³ College of Astronomy and Space Sciences, University of Chinese Academy of Sciences, Beijing 100049, China

⁴ WHU-NAOC Joint Center for Astronomy, Wuhan University, Wuhan, Hubei 430072, China

of the solar magnetic reconnection. However, for stellar flares, their energies are much larger than those of solar flares (Walkowicz et al. 2011; Maehara et al. 2012; Yang & Liu 2019), and their durations are much shorter than expected values deduced from solar flares (Namekata et al. 2017). There could be some differences between solar and stellar coronae, such as the flaring activity and coronal plasma densities (e.g., Testa et al. 2004). In addition, it is still on debate whether the candidate heating mechanism for stellar coronae (e.g., “nanoflares”) is effective for the heating of the solar corona. Most of our understanding on stellar activity and atmospheric structure are from the Sun, and detailed studies of stellar activity can also help re-examine the solar physics.

A large sample covering different type of stars, with stellar activities estimated from a uniform procedure, can help us doing detailed investigation of the physical properties of stellar activity, and provide potential diagnostics of heating mechanisms. Stellar activity has been explored in the X-ray regime for nearly forty years (Vaiana et al. 1981; Schmitt et al. 1985; Pizzolato et al. 2003; Mamajek & Hillenbrand 2008). Benefited from new X-ray missions with high spatial resolution and low background noise, our knowledge of stellar coronae and activity can be continually refined. In this paper, we use the *Chandra* data archive and the *Gaia* DR2 to provide a large sample of stars with accurately estimated X-ray activities. In Section 2, we describe the sample selection and data reduction process. Section 3 presents the stellar activity investigations, including the X-ray activity in different stellar types, the relation between X-ray activity and hardness ratio, and the X-ray flux variation. In Section 4, we show some analyses and application examples of our catalog.

2. SAMPLE SELECTION AND DATA REDUCTION

2.1. Sample Selection

The unprecedented subarcsecond spatial resolution of *Chandra* telescope allows X-ray sources to be unambiguously matched to their optical counterparts. Our primary database is the *Chandra* point source catalog (Wang et al. 2016), which includes 217,828 distinct X-ray sources with 363,530 detections. The *Gaia* DR2 released about 1.33 billion celestial objects with estimated distances (Bailer-Jones et al. 2018), which can be used to evaluate X-ray luminosity and bolometric luminosity of the stars. Firstly, we cross-matched the *Chandra* point source catalog and the *Gaia* DR2 catalog, using a radius of $3''$. In some cases there are multiple matches, and we only selected the closest neighbour as the counterpart. This led to more than 60 thousand unique sources with *Chandra* detections.

Secondly, we used a machine learning method (Bai et al. 2019) to classify possible contamination from non-stellar objects, such as galaxy and quasi-stellar object (QSO). The classifier uses nine colors (i.e., $g - r$, $r - i$, $i - J$, $J - H$, $H - K_s$, $K_s - W1$, $W1 - W2$, $w1mag_1 - w1mag_3$, $w2mag_1 - w2mag_3$), spanning from optical to far-infrared bands. In order to obtain these colors, we cross-matched the ~ 60 thousand sources with the Pan-STARRS DR1 (hereafter PS1; Chambers et al. 2016), UCAC4 (Zacharias et al.

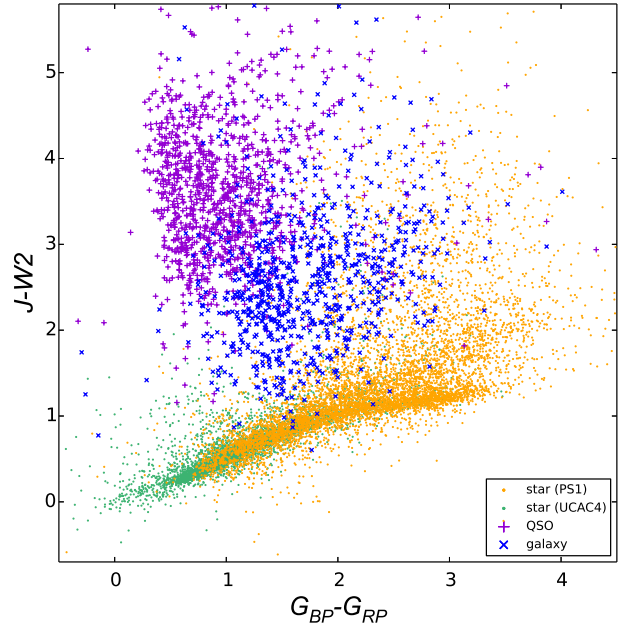


Figure 1. Color-color diagram of the initial sample. The yellow and green points represent stars with PS1 and UCAC4 magnitudes, respectively. The purple pluses and blue crosses show the distinguished QSOs and galaxies, respectively.

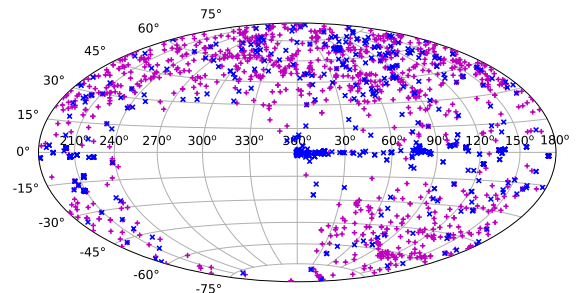


Figure 2. Sky distribution of the classified QSOs (plus) and galaxies (cross), in Galactic coordinates.

2013), and WISE All-Sky (Cutri et al. 2012) catalogs, by using the TOPCAT⁵ and CasJobs⁶. The matching radius is $3''$, and only the closest counterpart was selected for the multiple coincidences. We first collected the g , r , and i magnitudes from the PS1. For objects without PS1 observations, we derived the magnitudes from the UCAC4 catalog. The WISE All-Sky data release includes the 2MASS magnitudes and WISE magnitudes. The $W1$ and $W2$ magnitudes are the $w1(2)mpro$ magnitudes in the WISE catalog; the $w1(2)mag_1$ and $w1(2)mag_3$ are magnitudes measured with circular apertures of radii of $5.5''$ and $11''$, and the differential aperture magnitude is expected to have different distributions for point and extended sources (Bilicki et al. 2014; Krakowski et al. 2016). Furthermore, we set the saturate

⁵ <http://www.star.bris.ac.uk/%7EEmbt/topcat>

⁶ <http://skyserver.sdss.org/CasJobs>

tion thresholds for these different surveys: $W2 = 6.7$ mag for WISE⁷; $K_S = 8$ mag for 2MASS⁸; $g = 14$ mag, $r = 14$ mag, and $i = 14$ mag for PS1⁹; $V = 7$ mag for UCAC4¹⁰. We also set the detection limits using the g , r , and i magnitudes (~ 23.2 mag) for PS1 observations, and the V magnitude (~ 17 mag) for UCAC4 observations, respectively. This method led to more than 11000 stars, ~ 800 galaxies, and ~ 1100 QSOs (Figure 1). Figure 2 shows the sky distribution of the extragalactic sources in Galactic coordinates. About 490 galaxies lie across the Galactic plane ($-10^\circ \leq l \leq 10^\circ$). Among these sources, about 150/250 sources have a neighbour within $3''/5''$, indicating their photometry may suffer from a contamination by nearby objects. Considering that the crowding can result in inaccurate photometry that may move the color index towards the blue band (Gaia Collaboration et al. 2018a,b), the classification of these galaxies may be unreliable.

Thirdly, we collected the extinction from the Pan-STARRS 3D dust map, which is constructed with the high-quality stellar photometry of 800 million stars from PS1 and 2MASS (Green et al. 2015). The reddening values $E(B - V)$ were used to estimate the absolute optical magnitude and the unabsorbed X-ray flux.

Fourthly, in order to have accurate distance estimations, we excluded the objects with relative parallax uncertainties larger than 0.2, although this may introduce biases towards bright nearby sources in our sample (Luri et al. 2018). Furthermore, we removed those objects with SIMBAD classification as white dwarf, planet nebula, binary, galaxy, and QSO. Finally, there are more than 5900 stars left in our sample.

2.2. Chandra Data Analysis

We extracted the X-ray information (i.e., net counts and count rates in different bands) for each star in each detection from the *Chandra* point source catalog (Wang et al. 2016). The hardness ratios ($HR1$ and $HR2$) for each detection were then calculated with the net photon counts for the three bands defined by Prestwich et al. (2003), i.e., the soft band (S: 0.3–1.0 keV), the medium band (M: 1.0–2.0 keV), and the hard band (H: 2.0–8.0 keV). The $HR1$ and $HR2$ were defined as $(M-S)/(M+S)$ and $(H-M)/(H+M)$, respectively.

We converted the net count rate (0.3–8 keV) into unabsorbed flux using PIMMS¹¹ with an APEC model. APEC is a model of emission spectrum from collisionally ionized diffuse gas in XSPEC and is often used to describe the X-ray emission of stars. First, we constructed spectral tracks of absorbed APEC spectra with the coronal temperature covering from $\log T(\text{K}) = 6$ to 8.5 with $\Delta \log T = 0.1$, and the hydrogen column density N_{H} (cm^{-2}) covering from 0 to 10^{23} with $\Delta \log N_{\text{H}} = 0.1$. The HR s of each model in the resulting grid was calculated. Second, we derived the coronal temperature, for each detection of each object in our catalog, by selecting the model with closest HR s (Figure 3). The models

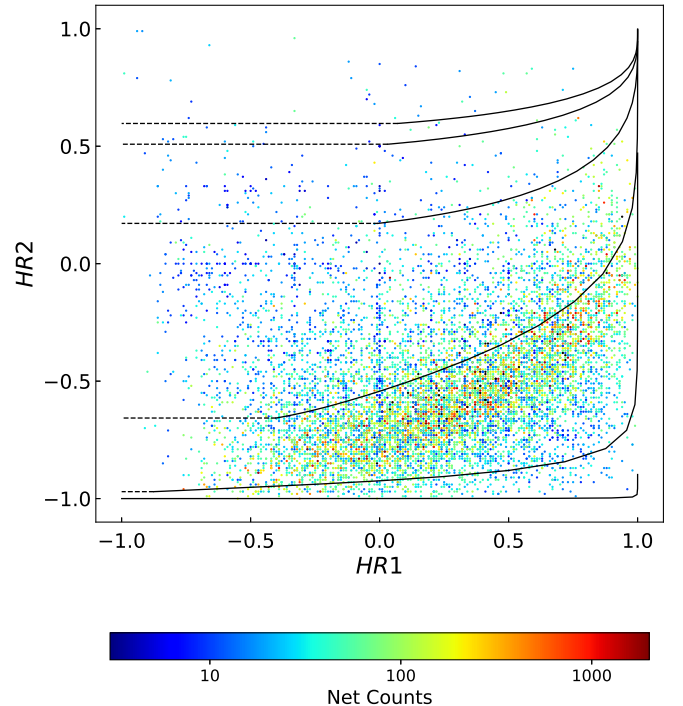


Figure 3. X-ray HR diagrams for all *Chandra* detections. Overplotted are examples of thermal spectra (APEC model, red lines) with temperatures of $\log T(\text{K}) = 6.0$ (bottom), 6.5, 7.0, 7.5, 8.0, 8.5 (top). These lines are obtained with N_{H} varying from 0 to 10^{23} cm^{-2} . The blue horizontal lines are extension of the red lines.

(solid lines) can not predict temperatures of the sources with low $HR1$ values (in the left part of Figure 3). The low $HR1$ values can be mostly due to statistical fluctuation of the photons, especially for low-count detections. A few sources show a soft excess (i.e., an additional thermal component) in their spectra, which can also reduce $HR1$ values (see Appendix A). Here we simply extended each APEC model (dashed line) to derive the temperatures of those sources. Third, we determined the observation cycle (or AO) for each detection, which was used in PIMMS to convert the count rate to flux for *Chandra* archive data. Finally, for each detection, we calculated the flux using the APEC model ($Z = 0.5 Z_{\odot}$) with individual coronal temperature and N_{H} , the latter of which was estimated from individual optical extinction (Zhu et al. 2017):

$$N_{\text{H}}(\text{cm}^{-2}) = 2.19 \times 10^{21} A_V(\text{mag}). \quad (1)$$

Before we estimated an averaged quiescent flux for each star, we removed those detections with X-ray flares. We first used the standard nonparametric Kolmogorov–Smirnov (K–S) test to quantitatively test the source variability during each observation. The observations with variable light curve were identified with K–S probability $P_{\text{K-S}} < 0.1$. Then we applied Bayesian block analysis (*astropy.stats.bayesian_blocks*; Scargle et al. 2013) to these observations to detect flares. By operating on unbinned events, this method can detect and characterize

⁷ http://wise2.ipac.caltech.edu/docs/release/allsky/expsup/sec6_3d.html

⁸ https://old.ipac.caltech.edu/2mass/releases/allsky/doc/sec1_6b.html

⁹ <https://panstarrs.stsci.edu>

¹⁰ <https://www.aavso.org/apass>

¹¹ <http://cxc.harvard.edu/toolkit/pimms.jsp>

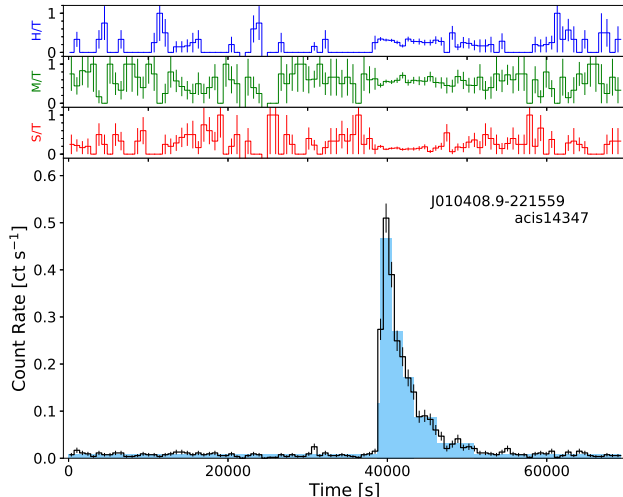


Figure 4. An example of the light curve of stellar X-ray flare. The *S*, *M*, and *H* represent the soft (0.3–1 keV), medium (1–2 keV), and hard (2–8 keV) bands, respectively. The blue histograms show the Bayesian blocks.

local variance in the count rate, and works well in flare identification (e.g., Neilsen et al. 2013; Ponti et al. 2015). The false alarm probability is set as $p_0 = 0.01$. A detailed study of the X-ray flares in our sample is currently in preparation as an independent work. The vignetting-corrected net count rate and unabsorbed flux for each observation are listed in Table 1. Finally, we calculated an exposure-weighted averaged X-ray flux for each star. The X-ray luminosity (L_X) was determined from the unabsorbed averaged flux (f_X) and distance (Table 2).

2.3. Stellar parameters and classification

To derive individual stellar parameters (i.e., effective temperature, surface gravity, and metallicity), our primary choice is the Large Sky Area Multi-Object Fiber Spectroscopic Telescope (hereafter LAMOST, also called the Guo Shou Jing Telescope) data base. LAMOST a reflecting Schmidt telescope, with an effective aperture of 4 m and a field of view of 5 degrees (Cui et al. 2012; Zhao et al. 2012). The LAMOST DR7 dataset released more than 14 million spectra, and presented parameter estimations for more than 6 million A, F, G, and K stars. For stars not included in the LAMOST DR7 catalog, we adopted the parameters ($teff50$, $logg50$, $met50$) from Anders et al. (2019), who derived Bayesian stellar parameters and distances for 265 million stars using the code StarHorse, based on the combination of *Gaia* DR2 and the photometric catalogs of PS1, 2MASS, and AllWISE. There are 447 and 3550 objects in common between our sample and LAMOST DR7 catalog and Anders et al. (2019), respectively. We defined the stars with parameter estimations as the “parameter” sample, and other stars as the “non-parameter” sample. Using the effective temperatures, we classified the “parameter” sample into different subclasses: O type with $T_{\text{eff}} \geq 30000$ K; B type with $10000 \text{ K} \leq T_{\text{eff}} < 30000$ K; A type with $7500 \text{ K} \leq T_{\text{eff}} < 10000$ K; F type with $6000 \text{ K} \leq T_{\text{eff}} < 7500$ K; G type with $5200 \text{ K} \leq T_{\text{eff}} < 6000$ K; K type with $3700 \text{ K} \leq T_{\text{eff}} < 5200$ K; M type with $T_{\text{eff}} < 3700$ K.

We further classified the sample into giants, YSOs, and

Table 1
Individual *Chandra* observation for stars in our sample.

Object	ObsID	MJD	Count Rate	Flux
(1)	(2)	(3)	(4)	(5)
		(day)	ks^{-1}	$(10^{-15} \text{ erg cm}^{-2} \text{ s}^{-1})$
J000012.8+622947	acis2810	52531.383	0.92 ± 0.21	11 ± 2
J000100.1-245742	acis13394	55784.056	0.32 ± 0.11	2.8 ± 1.0
J000101.9-250431	acis13394	55784.056	0.21 ± 0.09	1.8 ± 0.8
J000136.1+130639	acis6978	54075.017	23 ± 1	175 ± 7
J000136.1+130639	acis8491	54124.292	12 ± 1	110 ± 8
J000238.8+255219	acis5610	53394.483	10 ± 2	40 ± 6
J000611.4+725929	acis3835	52742.424	1.8 ± 0.3	17 ± 2
J000645.6+730635	acis3835	52742.424	0.31 ± 0.14	2.4 ± 1.1
J000753.8+512400	acis8942	54544.217	0.67 ± 0.15	3.5 ± 0.8
J000759.3+512655	acis8942	54544.217	1.8 ± 0.3	7.3 ± 1.0
J000833.8+512412	acis8942	54544.217	0.46 ± 0.15	2.1 ± 0.7
J000835.3+512142	acis8942	54544.217	0.98 ± 0.21	3.8 ± 0.8
J000836.5+512616	acis8942	54544.217	0.29 ± 0.14	1.6 ± 0.8
J000849.5+512514	acis8942	54544.217	5.7 ± 0.5	24 ± 2
J001051.6-120543	acis15061	56448.701	1.4 ± 0.5	9.6 ± 3.7
J001116.8-151526	acis6105	53549.484	1.3 ± 0.3	14 ± 3
J001123.9-151541	acis6105	53549.484	0.56 ± 0.19	4.1 ± 1.4
J001144.7+522859	acis15318	56453.998	1.4 ± 0.3	17 ± 3
J001145.8-285501	acis5797	53610.327	0.64 ± 0.29	7.0 ± 3.2
J001147.4-152319	acis6105	53549.484	2.0 ± 0.3	13 ± 2

(This table is available in its entirety in machine-readable and Virtual Observatory (VO) forms in the online journal. A portion is shown here for guidance regarding its form and content.)

dwarfs. First, a star was considered as a giant if the $\log g$ value is smaller than that specified in the following algorithm (Ciardi et al. 2011):

$$\log g < \begin{cases} 3.5 & \text{if } T_{\text{eff}} \geq 6000, \\ 4.0 & \text{if } T_{\text{eff}} \leq 4250, \\ 5.2 - 2.8 \times 10^{-4} T_{\text{eff}} & \text{if } 4250 \leq T_{\text{eff}} \leq 6000. \end{cases} \quad (2)$$

This leads to 685 giants and 3312 dwarfs and YSOs. We then cross-matched our sample with the catalogs in Marton et al. (2016, 2019). By using the 2MASS and WISE photometric data, combined with *Planck* dust opacity values, Marton et al. (2016) presented a catalog of Class I/II and III YSO candidates with the support vector machine method. By adding the *Gaia* data base, Marton et al. (2019) presented a new catalog, classifying more than 100 million sources into four classes: YSOs, extragalactic objects, main-sequence stars, and evolved stars. There are 1100 objects in common between our sample and these catalogs, including 68 giants, 900 YSOs, and 132 dwarfs. For sources in Marton et al. (2019), only those with reliable classification probability ($P > 90\%$) were selected. Sometimes one star has different classifications from above methods, we preferentially adopted the classification by using the $\log g$ value from LAMOST DR7 and Anders et al. (2019), followed by the classification of Marton et al. (2019). We classified a total of 697 giants.

Second, we defined some criteria to classify more new YSOs. As Marton et al. (2019) reported, 99% of the

known YSOs are located in the regions where the dust opacity value is higher than 1.3×10^{-5} . Thus we labeled as YSO candidates those sources that meet the requirements: (1) $\tau > 1.3 \times 10^{-5}$ and (2) $J - H > 1 - (H - K_S)$ or $W1 - W2 > 0.04$ (See Appendix B for more details). In addition, considering that there may be many AGB stars with $W2 - W3 < 1$ (Koenig & Leisawitz 2014), we add one criterion $W2 - W3 \geq 1$ for the “non-parameter” sample. With the constraints of colors and dust opacity, we classified additional ≈ 300 stars to be YSOs. We finally categorized 1196 YSOs.

Third, for the “parameter” sample, if they were not classified as YSOs or giants from above steps and if their dust opacity values are lower than 1.3×10^{-5} , we flagged them as main-sequence dwarfs.

In summary, the giants were collected from the “parameter” sample and Marton et al. (2019); the YSOs were classified from previous studies (Marton et al. 2016, 2019) and our criteria; for the dwarfs, one part was selected from Marton et al. (2019), and the other part was classified from the “parameter” sample. Figure 5 summarizes the steps in a flowchart for reference.

At the end, we presented stellar classifications for 3005 sources in our sample, including 1196 YSOs, 1112 dwarfs, and 697 giants. Among these sources, 432 YSOs, 1111 dwarfs, and 695 giants have parameter estimations. We defined these 2238 sources as the “A-class” sample, which will be used for following analysis.

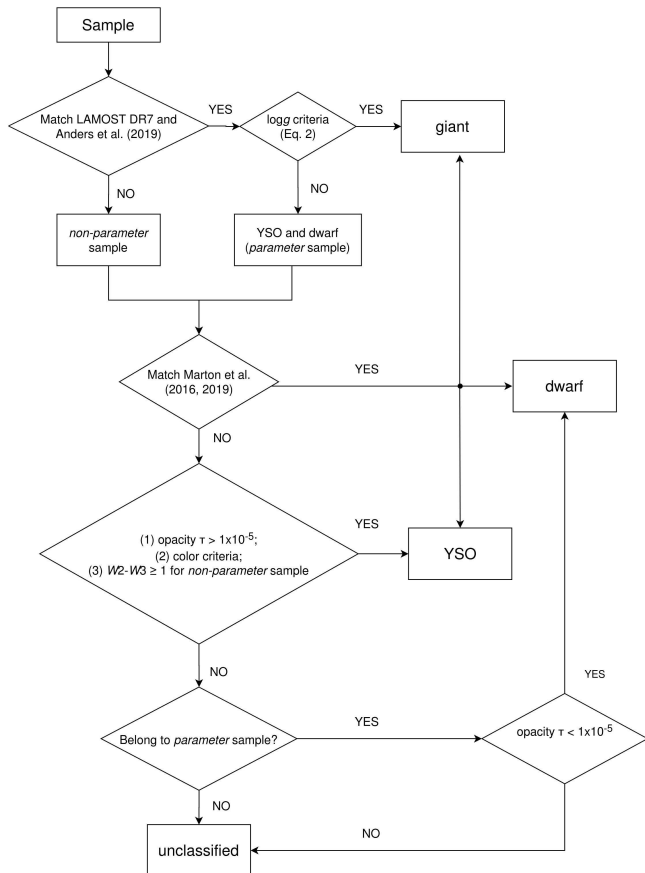


Figure 5. Summary flowchart of the stellar classification process in this paper.

3. STELLAR X-RAY ACTIVITY

3.1. X-ray Activity in Different Stellar Types

X-ray emission is prevalent among almost all stellar classes (e.g., Stocke et al. 1991), although with different mechanisms (see Güdel 2004, for a review). For the hot and massive early-type stars, the emitted X-rays arise from either small-scale shocks in their winds or collisions between the wind and circumstellar material (Lucy & White 1980; Parkin et al. 2009). For late-type stars, the X-ray emission is attributed to the presence of a magnetic corona (Vaiana et al. 1981). The X-ray emission of YSOs may be from accretion shock, star-disk interaction, or solar-like corona (e.g., Preibisch et al. 2005). In this paper, we used the ratio of X-ray-to-bolometric luminosities ($R_X = L_X/L_{\text{bol}}$) as the X-ray activity indicators. We used the PARSEC theoretical models to determine the bolometric luminosity (see Appendix C).

Figure 6 displays the distributions of L_X and R_X for different stellar types in our “A-class” sample. For each stellar type, giants have the highest luminosities up to 10^{32} – 10^{33} erg s $^{-1}$. For G and K stars, we ran a K-S test (*scipy.stats.ks_2samp*) to check the similarity of L_X distributions. Since the YSOs, dwarfs, and giants have different numbers, we randomly selected ≈ 100 objects for each class and calculated the P_{K-S} values. The selection and calculation was repeated 10^4 times, allowing us to have an averaged P_{K-S} estimation. For giants and dwarfs, the P_{K-S} values are smaller than 10^{-10} for both G and K stars, indicating a different distribution; for YSOs and dwarfs, the P_{K-S} values are $\approx 6 \times 10^{-4}$ (G stars) and ≈ 0.06 (K stars), respectively.

In previous studies, YSOs were found to have X-ray luminosities 10 – 10^4 above those typically seen in main-sequence stars (e.g., Feigelson et al. 2002; Preibisch et al. 2005). However, no such notable difference can be seen in Figure 6. This may be explained by the incompleteness of our dwarf sample. Take K stars as an example, previous observations (*ROSAT*; 0.1–2.4 keV) showed that the field dwarfs have X-ray luminosities ranging from $\approx 6 \times 10^{26}$ erg/s to $\approx 2 \times 10^{30}$ erg/s, while the dwarfs in open clusters Pleiades and Hyades have X-ray luminosities spanning from $\approx 3 \times 10^{28}$ erg/s to $\approx 4 \times 10^{30}$ erg/s (Wright et al. 2011). The X-ray luminosities (*Chandra*; 0.5–8 keV) of pre-main-sequence K5–7 stars in the Orion nebula are from $\approx 3 \times 10^{29}$ erg/s to $\approx 2 \times 10^{31}$ erg/s (Wolk et al. 2005). It seems that most of the K dwarfs in our catalog are in the high-luminosity tail of the L_X distribution of Galactic K stars. This may be due to the *Chandra* observation mode and our sample selection methods. For example, the requirement of *WISE* photometry may remove a number of dwarfs.

In general, the R_X distributions are similar among different classes. For giants and dwarfs, the P_{K-S} values are about 0.14 and 0.20, respectively. For YSOs and dwarfs, the P_{K-S} values are smaller than 0.01 for both G and K stars. More YSOs have higher R_X values than the dwarfs in the same stellar type.

We noted that there is a large difference between the number of M-type YSOs and dwarfs. Among the 161 M-type YSOs with parameter estimations, about half is from Marton et al. (2016, 2019) and the other half is

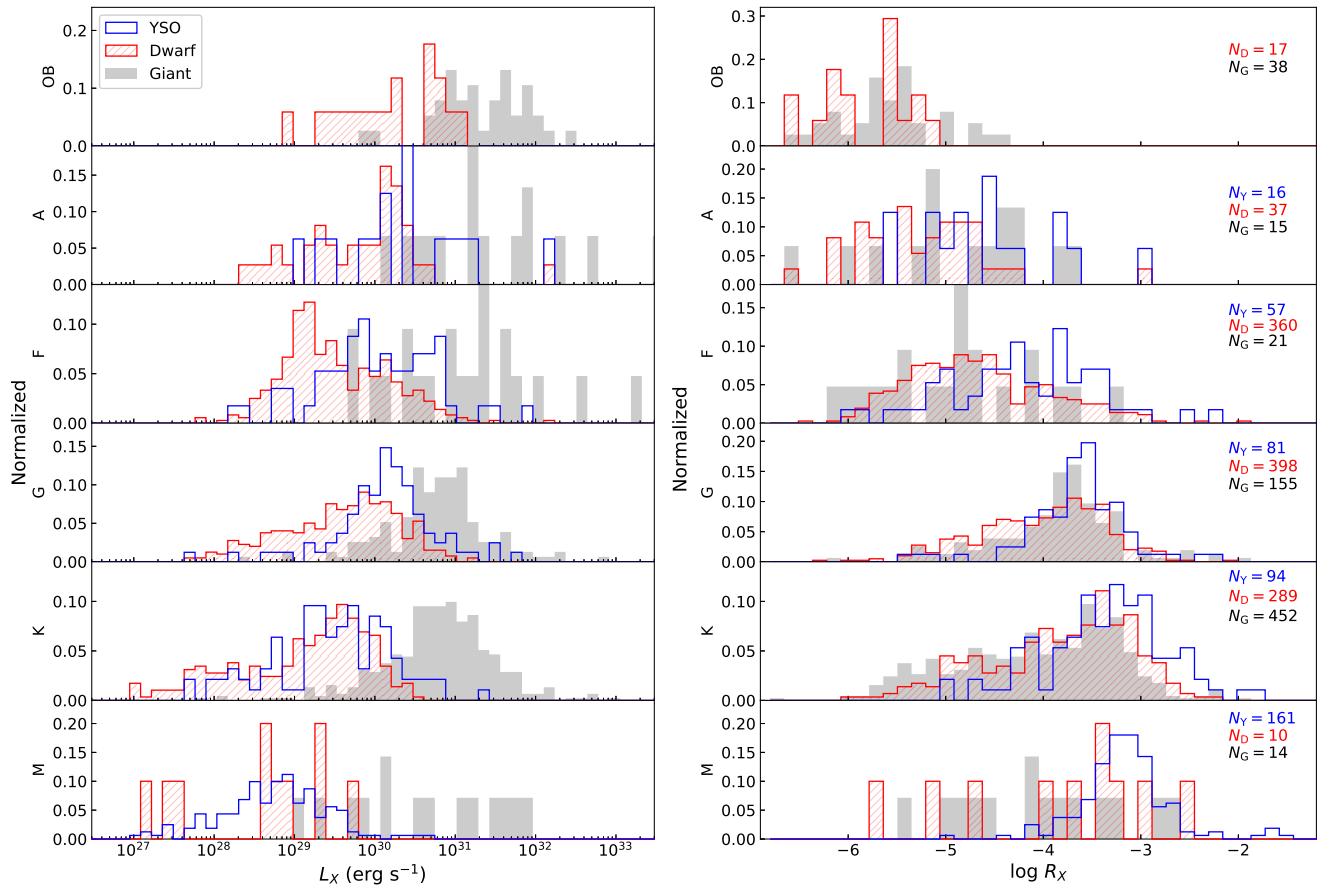


Figure 6. Left panel: Histograms showing the distributions of L_X for stars from OB to M type. Right panel: Histograms showing the distributions of R_X for stars of spectral type OB through M.

picked out with our criteria. One caveat is that about 50 ones have $W2 - W3 < 1$, some of which may be wrongly classified (i.e., contaminated by dwarfs or giants). However, the statistical distributions will not be much affected.

3.2. X-ray Activity and Hardness Ratio

X-ray emission of late-type stars is from solar-like corona, which suggests a relation between stellar X-ray activity and coronal activity. The positive correlation between X-ray luminosity and coronal temperature has been explored (e.g., Schmitt et al. 1995; Güdel 2004), which can be referred on the basis of a “loop” model for stellar coronae (Vaiana 1983). Active stars with more efficient dynamo have stronger magnetic fields in the corona, and thus higher rate of field line reconnections and flares. This results in higher coronal temperatures and a larger plasma density of energetic electrons. Here we take the X-ray HR to track the coronal temperature for late-type stars. There is a clear positive correlation between L_X and $HR1$ (Figure 7), which means stronger X-ray emitters have higher coronal temperatures. Most YSOs are in the saturated regime, with a constant R_X value ($\log R_X \approx -3$) when $HR1$ varies (Figure 8). We performed a Spearman correlation test (*scipy.stats.spearmanr*) for all these relations. Then linear regression fits were done for these relations with higher correlation coefficients (Table 3).

The YSOs and dwarfs share similar $HR1$ distribution (Figure 9), while for all late stellar types (from F to K), there are giants showing very high $HR1$ values, which are good candidates possessing high-temperature corona. A K-S test was also run for the $HR1$ distributions. For YSOs and dwarfs, the P_{K-S} values are $\approx 2 \times 10^{-4}$ (G stars) and ≈ 0.05 (K stars), respectively; for giants and dwarfs, the P_{K-S} values are smaller than 10^{-7} for both G and K stars. Again, we remind that the samples of each stellar type are incomplete.

3.3. X-ray Flux Variation

Stellar X-ray emission is variable (Soderblom 2010; Stelzer 2017). The most prominent signature of the variability is flares, which usually show sudden and intense brightness increase and decay. The short X-ray variability can be also due to rotational modulation of the structural inhomogeneity of magnetic field (Marino et al. 2003). Significant correlations have been found between the positions of active longitudes in the activity diagnostics, including the X-ray light curve, star spot, and magnetic field maps (Hussain et al. 2007). The long-term X-ray variability may reflect magnetic dynamo cycles (Sanz-Forcada et al. 2013; Ayres 2014). However, there are only few sources showing X-ray cycles, since long-term X-ray monitoring is not easily feasible and it is hard to detect dynamo cycle in the X-ray band (Stelzer 2017). For YSOs, the

Table 2
Main properties for the stars in our sample.

Object	RA	Dec	Class	D	$E(B - V)$	f_X	L_X	$\log R_X$	$HR1$	$HR2$
(1)	($^\circ$)	($^\circ$)	(4)	(pc)	(mag)	(10^{-15} erg cm $^{-2}$ s $^{-1}$)	(erg s $^{-1}$)	(9)	(10)	(11)
J000012.8+622947	0.05374	62.49657	G	899 $^{+21}_{-20}$	0.26	11 \pm 2	1.0e+30 \pm 2.4e+29	-4.0 \pm 0.1	0.59 \pm 0.22	-0.84 \pm 0.29
J000100.1-245742	0.25066	-24.96192	M	376 $^{+21}_{-19}$	0.02	2.8 \pm 1.0	4.7e+28 \pm 1.6e+28	-3.52 \pm 0.15	0.15 \pm 0.4	-0.7 \pm 0.52
J000101.9-250431	0.25818	-25.07535	Kd	242 $^{+2}_{-2}$	0.01	1.8 \pm 0.8	1.3e+28 \pm 5.7e+27	-5.0 \pm 0.2	0.0 \pm 0.57	-0.38 \pm 0.74
J000136.1+130639	0.40042	13.11095	Fd	381 $^{+7}_{-6}$	0.08	149 \pm 5	2.6e+30 \pm 9.6e+28	-3.74 \pm 0.02	0.21 \pm 0.04	-0.66 \pm 0.04
J000238.8+255219	0.66206	25.87221	K	703 $^{+30}_{-27}$	0.03	40 \pm 6	2.4e+30 \pm 3.6e+29	-2.66 \pm 0.07	0.09 \pm 0.17	-0.71 \pm 0.18
J000611.4+725929	1.54788	72.99162	G	1680 $^{+138}_{-119}$	0.37	17 \pm 2	5.7e+30 \pm 7.8e+29	-3.09 \pm 0.06	-0.01 \pm 0.15	-0.42 \pm 0.2
J000645.6+730635	1.69003	73.10997	K	368 $^{+3}_{-3}$	0.33	2.4 \pm 1.1	3.9e+28 \pm 1.8e+28	-4.4 \pm 0.2	-0.1 \pm 0.52	-0.5 \pm 0.83
J000753.8+512400	1.97436	51.40010	Ky	597 $^{+28}_{-26}$	0.12	2.1 \pm 0.9	1.5e+29 \pm 3.4e+28	-3.48 \pm 0.1	-0.27 \pm 0.25	-0.47 \pm 0.43
J000759.3+512655	1.99728	51.44876	My	290 $^{+10}_{-10}$	0.05	3.8 \pm 1.8	7.4e+28 \pm 1.0e+28	-3.15 \pm 0.06	-0.19 \pm 0.15	-0.59 \pm 0.24
J000833.8+512412	2.14095	51.40359	Ad	434 $^{+8}_{-8}$	0.09	11 \pm 1	4.7e+28 \pm 1.6e+28	-6.53 \pm 0.15	-0.14 \pm 0.38	-0.76 \pm 0.61
J000835.3+512142	2.14724	51.36168	Kd	50 $^{+3}_{-2}$	0.01	3.5 \pm 0.8	1.1e+27 \pm 2.5e+26	-4.81 \pm 0.09	0.07 \pm 0.24	-0.83 \pm 0.29
J000836.5+512616	2.15234	51.43779	G	1497 $^{+115}_{-100}$	0.11	7.3 \pm 1.0	4.2e+29 \pm 2.1e+29	-4.14 \pm 0.22	-0.12 \pm 0.56	-0.91 \pm 1.17
J000849.5+512514	2.20651	51.42067	G	268 $^{+17}_{-15}$	0.07	205 \pm 4	2.1e+29 \pm 1.8e+28	-3.97 \pm 0.04	-0.11 \pm 0.09	-0.77 \pm 0.11
J001051.6-120543	2.71524	-12.09552	-	522 $^{+70}_{-56}$	0.02	2.1 \pm 0.7	3.1e+29 \pm 1.2e+29	-2.66 \pm 0.17	0.33 \pm 0.69	0.19 \pm 0.48
J001116.8-151526	2.82019	-15.25745	-	375 $^{+64}_{-48}$	0.02	3.8 \pm 0.8	2.4e+29 \pm 5.6e+28	-2.12 \pm 0.1	0.33 \pm 0.69	0.19 \pm 0.48
J001123.9-151541	2.84977	-15.26147	Kd	533 $^{+15}_{-14}$	0.02	1.6 \pm 0.8	1.4e+29 \pm 4.6e+28	-4.01 \pm 0.14	-0.21 \pm 0.39	-0.29 \pm 0.6
J001144.7+522859	2.93639	52.48312	K	393 $^{+10}_{-9}$	0.12	24 \pm 2	3.1e+29 \pm 6.1e+28	-3.04 \pm 0.08	0.28 \pm 0.21	-0.66 \pm 0.23
J001145.8-285501	2.94100	-28.91695	M	129 $^{+2}_{-2}$	0.01	9.6 \pm 3.7	1.4e+28 \pm 6.3e+27	-3.29 \pm 0.2	-0.42 \pm 0.73	0.41 \pm 0.76
J001147.4-152319	2.94754	-15.38880	K	374 $^{+13}_{-13}$	0.01	14 \pm 3	2.3e+29 \pm 3.0e+28	-3.08 \pm 0.06	-0.33 \pm 0.14	-0.53 \pm 0.23
J001152.5+523845	2.96884	52.64607	F	1303 $^{+77}_{-69}$	0.15	4.1 \pm 1.4	2.5e+30 \pm 7.5e+29	-3.31 \pm 0.13	0.36 \pm 0.33	-0.72 \pm 0.42

Note. — The columns are: (1) Object. (2) Right ascension in degree. (3) Declination in degree. (4) Stellar classification. (5) Distance from *Gaia* DR2 data. (6) $E(B - V)$ from PS1 3D map. (7) Averaged unabsorbed X-ray flux in the 0.3–8 keV. (8) X-ray luminosity in the 0.3–8 keV. (9) X-ray-to-bolometric luminosity ratio. (10) Hardness ratio $HR1 = (M - S)/(M + S)$. S/M represents background-subtracted counts in soft (0.3-1 keV) and medium (1-2 keV) bands. (11) Hardness ratio $HR2 = (H - M)/(H + M)$. M/H represents background-subtracted counts in medium (1-2 keV) and hard (2-8 keV) bands.

(This table is available in its entirety in machine-readable and Virtual Observatory (VO) forms in the online journal. A portion is shown here for guidance regarding its form and content.)

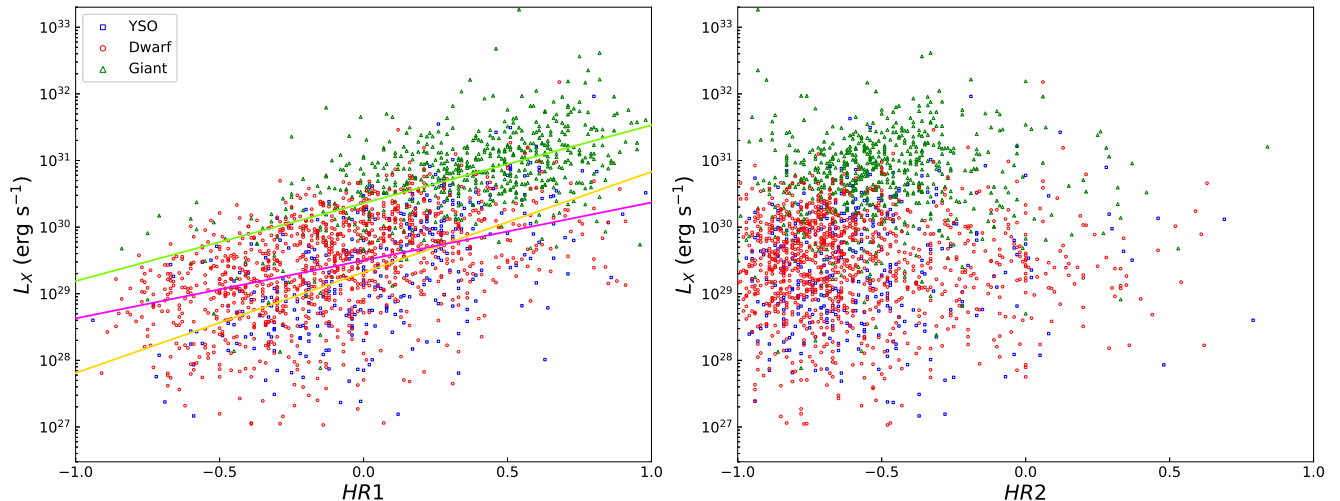


Figure 7. Left Panel: L_X versus $HR1$. The positive correlation means stronger X-ray emitters (higher L_X) have higher coronal temperatures. The yellow, purple, and green lines are the fits for YSOs, dwarfs, and giants, respectively. Right Panel: L_X versus $HR2$.

variability can also be related to the shocks and absorption associated with accretion disk and protostellar jets (e.g., Wolk et al. 2005; Flaccomio et al. 2006; Ustamujic et al. 2018; Guarcello et al. 2017).

In our sample, about 1400 stars were observed more

than once by *Chandra*. We calculated the relative flux variation as the standard flux variation during non-flare observations divided by the averaged flux. Most stars have small relative flux variation ($\sigma/f_X < 0.5$). The σ/f_X shows no clear relation with R_X and L_X (Figure

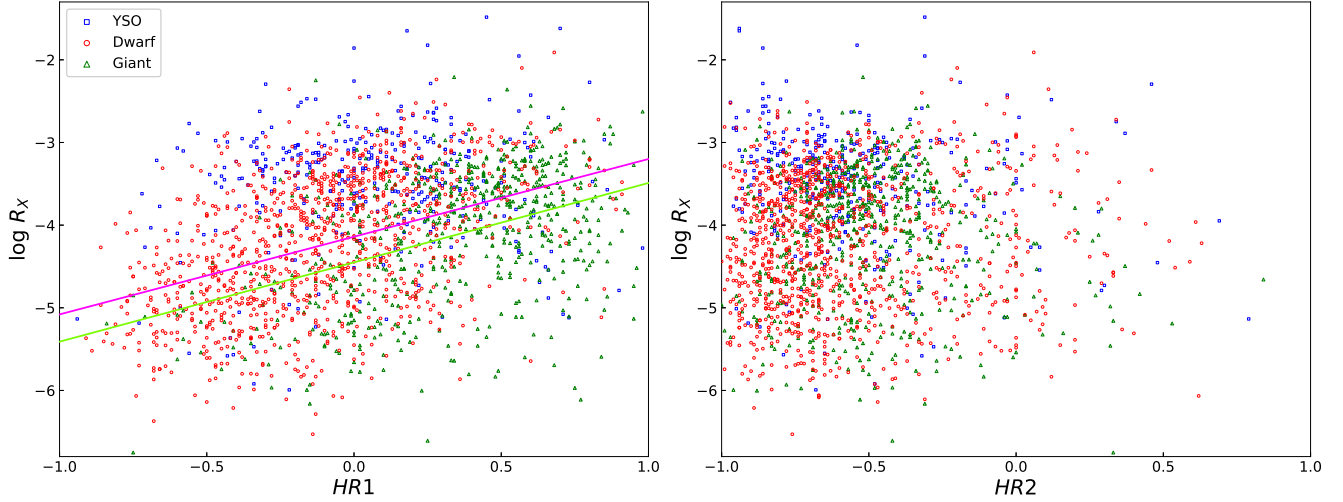


Figure 8. Left Panel: R_X versus $HR1$. The purple and green lines are the fits for dwarfs and giants, respectively. Right Panel: R_X versus $HR2$.

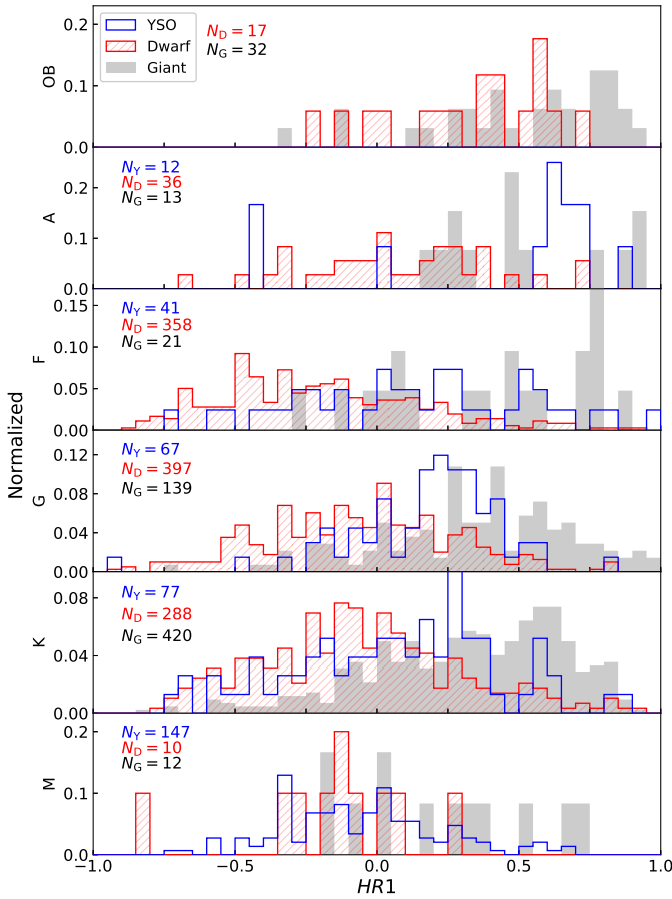


Figure 9. Histograms showing the distributions of $HR1$ for stars from OB to M type.

10). It also can be seen that the most variable sources are mainly YSOs. Figure 11 shows some examples of long-term light curves

4. ANALYSES AND SOME APPLICATIONS

Table 3
Fits to $\log(y) = a \times x + b$ in Logarithmic space.

y	x	Spearman correlation coefficient	a	b
(1)	(2)	(3)	(4)	(5)
YSO				
L_X	$HR1$	0.96	1.51 ± 0.17	29.32 ± 0.06
R_X	$HR1$	0.48	-	-
L_X	$HR2$	0.49	-	-
R_X	$HR2$	0.58	-	-
dwarf				
L_X	$HR1$	0.94	0.87 ± 0.08	29.50 ± 0.04
R_X	$HR1$	0.94	0.98 ± 0.08	-4.14 ± 0.04
L_X	$HR2$	0.16	-	-
R_X	$HR2$	0.36	-	-
giant				
L_X	$HR1$	0.99	1.17 ± 0.09	30.36 ± 0.04
R_X	$HR1$	0.85	0.96 ± 0.13	-4.45 ± 0.06
L_X	$HR2$	0.23	-	-
R_X	$HR2$	0.01	-	-

In this work, we provided a large sample with X-ray activities estimated from a uniform procedure, which can help do detailed investigation of the magnetic dynamo for different type stars. Here we give some possible scientific applications with this catalog. We remind that this catalog suffers from selection biases and is incomplete.

4.1. The Activity–Rotation Relation

Many studies have investigated the correlation between several coronal and chromospheric magnetic activity indicators and stellar rotation rate (e.g., Pizzolato et al. 2003; Mamajek & Hillenbrand 2008; Wright et al. 2011; Lehtinen et al. 2020). The Rossby number is used to trace the stellar rotation, which is de-

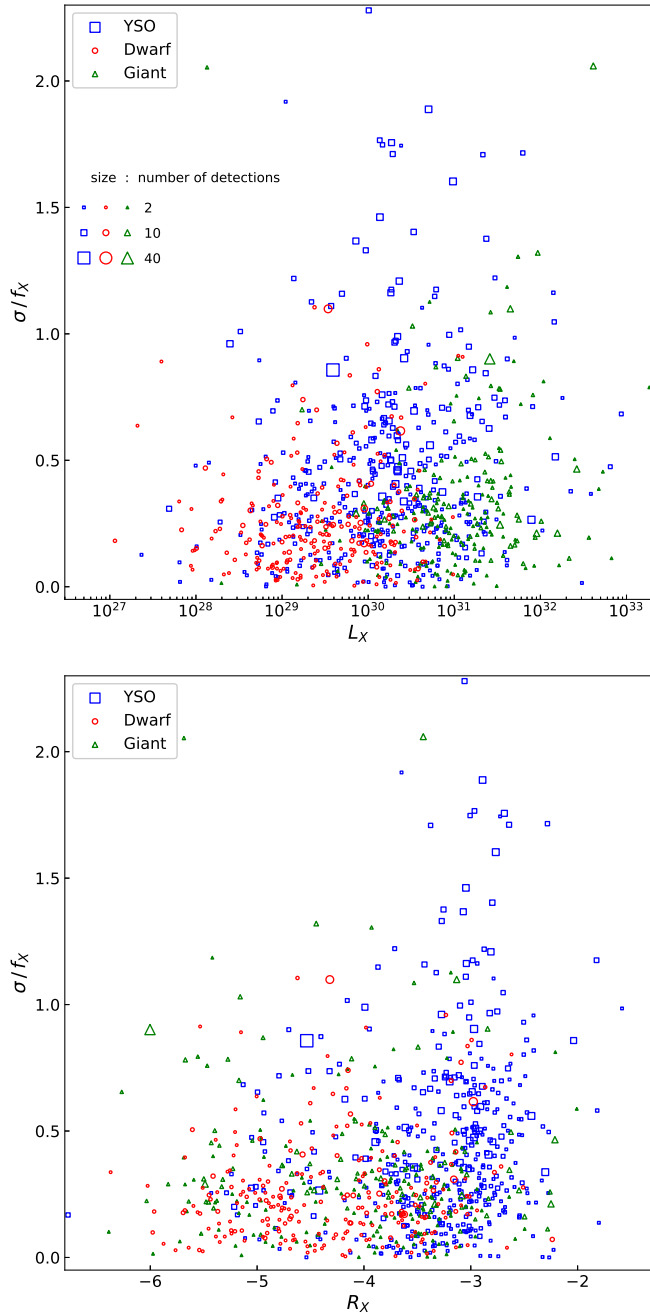


Figure 10. Top Panel: relative flux variation σ/f_X versus L_X . The symbol size represents the number of detections from *Chandra* data. Bottom Panel: relative flux variation σ/f_X versus R_X .

defined as the ratio of the rotation period to the convective turnover time ($Ro = P/\tau$).

In order to derive stellar rotation periods from *Kepler* data, we have developed an online platform, *Kepler Data Integration Platform*¹², which integrates query, view, and period calculation on the whole *Kepler* and *K2* data set (see Yang & Liu 2019, for details). In our sample, more than 900 stars were observed by the *Kepler* telescope, among which four are eclipsing binaries and about 100 ones show rotational modulation. By using the baseline-detrended light curve, their periods

¹² <http://kepler.bao.ac.cn>

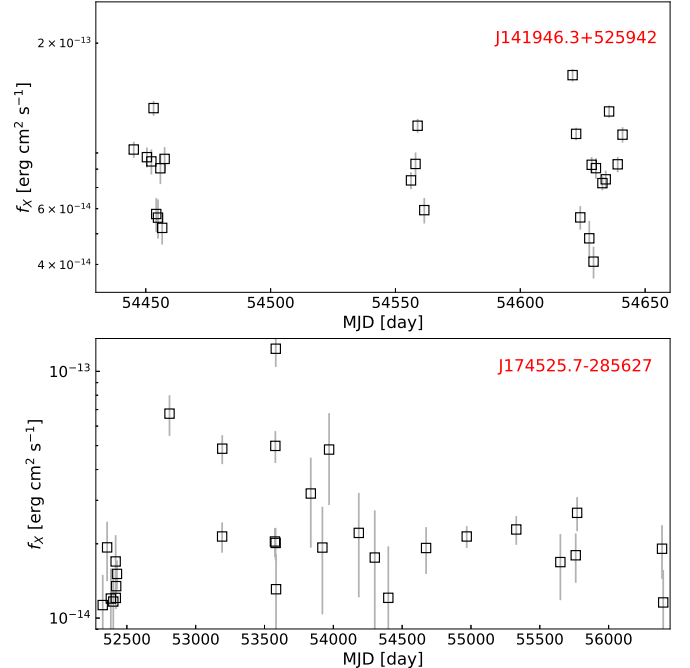


Figure 11. Examples of long-term X-ray light curves.

were computed with the Lomb–Scargle periodogram (see Gao et al. 2016; Yang & Liu 2019, for details).

The classical empirical estimate of τ from colors and effective temperatures works mainly for main-sequence dwarf (e.g., Noyes et al. 1984; Wright et al. 2011). Since our sample also includes YSOs and giants, we decided to derive the τ value using a grid of stellar evolution models from the YalePotsdam Stellar Isochrones (YAPSI) following Lehtinen et al. (2020). We did a fitting, by using the $\log T_{\text{eff}}$ and $\log g$ from LAMOST DR7 and Anders et al. (2019), to the model evolutionary tracks. The YAPSI models include five initial metallicities, $[Fe/H] = +0.3, 0.0, -0.5, -1.0,$ and -1.5 . For each star, we obtained best-fit models for these metallicities, and calculated the final τ value (and stellar radius) by linear interpolation to the metallicity from LAMOST DR7 and Anders et al. (2019).

Figure 12 shows R_X as a function of Ro . The dashed line is from Wright et al. (2011), but shifted to the left with a ratio of $Ro/3$, since we derived a ratio between the theoretical and empirical τ values around 3 (Lehtinen et al. 2020 obtained a ratio of ≈ 2.6). For each stellar spectral type, the X-ray activity increases with decreasing rotation period, following a well-known activity–rotation relation (Figure 13). Most M stars are located in the saturated regime, which is usually explained by the magnetic/dynamo saturation (Reiners et al. 2009) or a change in the dynamo configuration of the star (Wright et al. 2011).

There are some theories for the saturation (and super-saturation; Prosser et al. 1996) of stellar X-ray emission: a saturation of the dynamo itself (e.g., Gilman 1983; Vilhu & Walter 1987), a saturation of the filling factor of active regions on the stellar surface (Vilhu 1984; Solanki et al. 1997; Stępień et al. 2001), or centrifugal stripping of the corona (Jardine & Unruh 1999). The lack of observed saturation in chromospheric emission (Cardini & Cassatella 2007; Mamajek & Hillenbrand

2008; Marsden et al. 2009; Jackson & Jeffries 2010; Argiroffi et al. 2016) are in contrast with the idea that the dynamo itself saturates. Analogously, the scenario of a saturation of the filling factor was argued against by some observations of rotational modulation of X-ray emission (Marino et al. 2003) and small coronal filling factors (Testa et al. 2004) in saturated/supersaturated stars. In addition, compact and dense coronal loops are found far below the corotation radius of the supersaturated star VW Cephei (Huenemoerder et al. 2006), indicating that saturation is not necessarily caused by coronal stripping (Wright et al. 2011). These could suggest that saturation is due to a change in regime of the underlying dynamo.

Some recent studies (e.g., Reiners et al. 2014) reported that the rotation period alone suffices to determine the activity-rotation scaling, and the relation $L_X/L_{\text{bol}} \propto P_{\text{rot}}^{-2}R^{-4}$ optimally describes the non-saturated fraction of stars. However, Lehtinen et al. (2020) found that the dwarfs and giants are located in a single sequence in the unsaturated regime in relation to Rossby numbers, while they are clearly separated in the relations R'_{HK} versus P_{rot} and R'_{HK} versus $P_{\text{rot}}^{-2}R^{-4}$. In our sample, the giants, with longer rotation periods, do not well follow the relation R_X versus $P_{\text{rot}}^{-2}R^{-4}$ for dwarfs (Figure 14). More stars with accurate period estimations will help examine these relations.

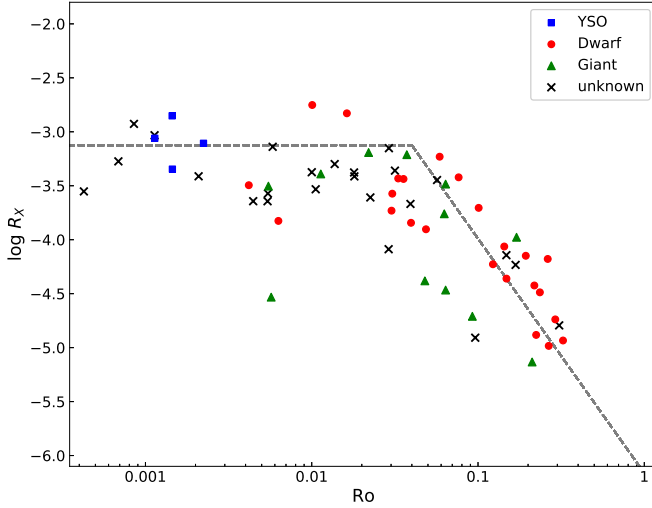


Figure 12. Relation between R_X and Ro for G, K, and M stars. The dashed line is from Wright et al. (2011), but shifted to left with a ratio of $Ro/3$.

4.2. Comparison with UV activity

A number of proxies have been used to study the activity occurring in the photosphere (star spots), chromosphere (Ca II HK; Mg II; H α ; optical flares; UV flux), and corona (X-ray emission). Observations have revealed good correlations between some of these proxies (e.g., Mamajek & Hillenbrand 2008; Stelzer et al. 2013), and the empirical scalings of these proxies with rotation period or Rossby number (e.g., Pallavicini et al. 1981; Pizzolato et al. 2003; Wright et al. 2011).

To have a comparison with the chromospheric activity,

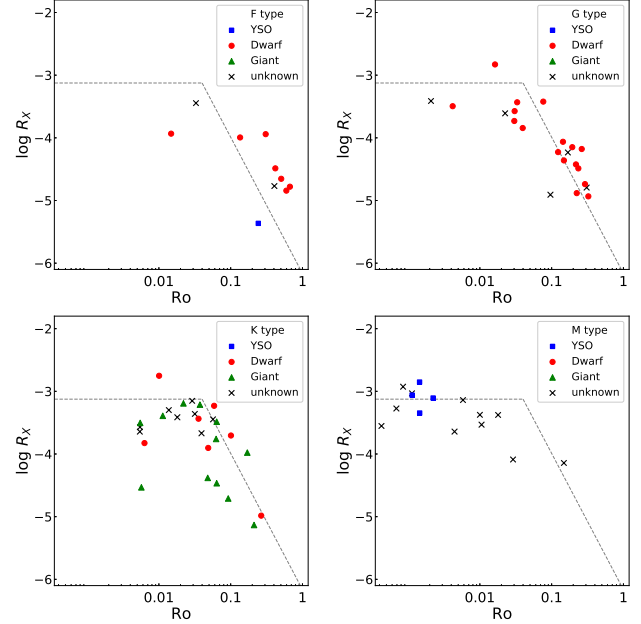


Figure 13. Relation between R_X and Ro for different type stars. The dashed line is from Wright et al. (2011), but shifted to left with a ratio of $Ro/3$.

we calculated the UV activity index as following:

$$R'_{UV} = \frac{f_{UV,exc}}{f_{bol}} = \frac{f_{UV,obs} - f_{UV,ph}}{f_{bol}}, \quad (3)$$

where ‘UV’ stands for the NUV and FUV bands, respectively. Here $f_{UV,exc}$ is the UV excess flux due to activity. The observed UV flux $f_{UV,obs}$ was estimated from the *GALEX* magnitude, by using the transformation relations¹³ as

$$f_{FUV,obs} = 10^{0.4 \times (18.82 - M_{FUV})} \times 1.40 \times 10^{-15} \times \delta\lambda_{FUV} \quad (4)$$

and

$$f_{NUV,obs} = 10^{0.4 \times (20.08 - M_{NUV})} \times 2.06 \times 10^{-16} \times \delta\lambda_{NUV}. \quad (5)$$

The M_{FUV} and M_{NUV} are absolute magnitudes, obtained from the observed magnitudes adopting the distance from *Gaia* DR2 and the extinction from the PS1 3D extinction map (See Section 2.1). The extinction coefficients were calculated as 8.11 (FUV) and 8.71 (NUV) following Cardelli et al. (1989). The $\delta\lambda_{FUV}$ and $\delta\lambda_{NUV}$ are the effective band width¹⁴ of the FUV and NUV filters (268 Å and 732 Å), respectively. The photospheric flux $f_{UV,ph}$, which means the photospheric contribution to the FUV and NUV emission, were estimated with the PARSEC model. Using the best fit model (see Appendix C), we derived the FUV and NUV magnitudes attributed to photospheric emission. The PARSEC models present the *GALEX* absolute magnitudes in VEGA system, therefore we first converted them into AB magnitudes (Bianchi 2011) and then converted them into fluxes using Equations (4) and (5). The bolometric flux f_{bol} was obtained with the bolometric luminosity from

¹³ https://asd.gsfc.nasa.gov/archive/galex/FAQ/counts_background.html

¹⁴ http://galexgi.gsfc.nasa.gov/docs/galex/Documents/ERO_data_description_2.htm

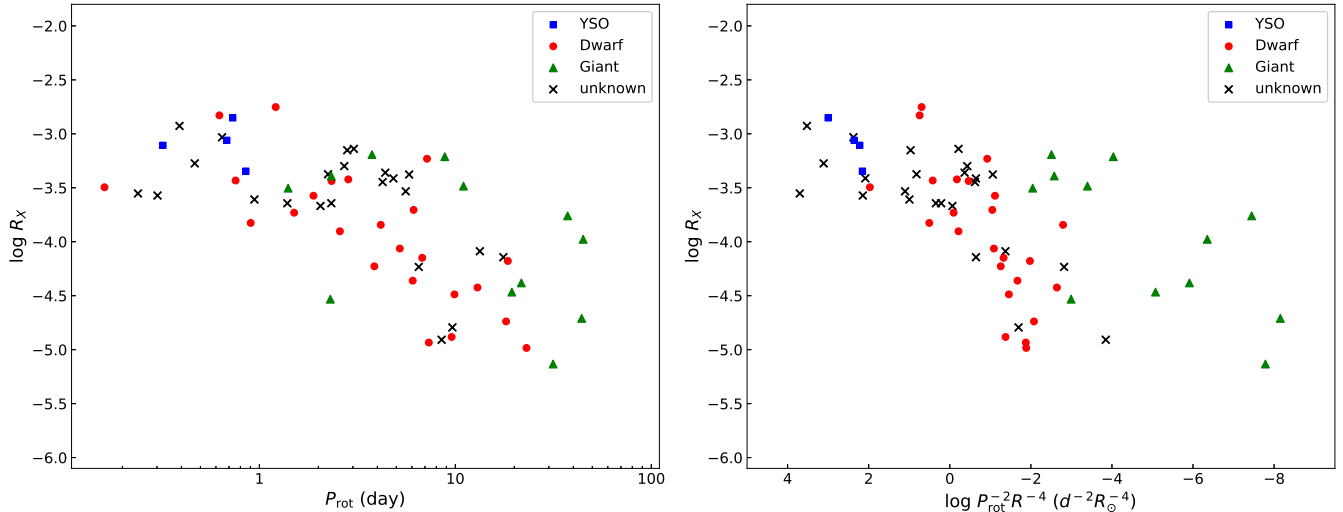


Figure 14. Left Panel: relation between R_X and rotational period for G, K, and M stars. Right Panel: relation between R_X and $P_{\text{rot}}^{-2}R^{-4}$ for G, K, and M stars.

the best fit PARSEC model. We calculated it using a distance of 10 pc. Table 4 lists the UV activity indexes.

We searched for the relations between FUV and NUV activities for different type stars (Figure 15). For F- and G-type stars, there is no clear relation, while for K and M stars, the FUV and NUV fluxes show an obvious positive relation (Stelzer et al. 2013). By using different stellar models (i.e., BT-Cond grid), Bai et al. (2018) calculated the UV excesses emission for millions of stars, and their sample showed similar trends. The lack of clear relation for F and G stars may be explained as the mixed populations with different ages. As can be seen in Figure 16, the F and G stars with lower FUV/NUV ratio may be older ones, while the young population show higher ratio of $\log(R'_{\text{FUV}}/R'_{\text{NUV}}) \gtrsim -1$ (see also Figure 12 in Richey-Yowell et al. 2019). Similar trends can be found in the comparisons between X-ray and UV activities (Figure 17 and 18). For G, K, and M stars, a positive relation can be seen between R'_X and R'_{FUV} , while only M stars show an obvious relation between R'_X and R'_{NUV} .

5. SUMMARY

We are carrying out systematic studies of stellar magnetic activities using a uniformly processed X-ray data set. By using the *Chandra* and *Gaia* DR2 data, we first presented a catalog of X-ray emitted stars and studied the X-ray activities of different type stars.

We used a machine learning method to select and exclude QSOs and galaxies from the initial sample, and divided the stellar sample into YSOs, dwarfs, and giants in different spectral types. We calculated the unabsorbed X-ray flux from count rate (taken from the *Chandra* point source catalog), using PIMMS with an APEC model. X-ray flares were detected with the Bayesian block analysis, and the entire observations with flares were removed. An exposure-weighted averaged flux was then calculated for each star, and the X-ray luminosity (L_X) was estimated adopting the *Gaia* DR2 distance. Finally, we calculated the X-ray-to-bolometric luminosity (R_X) as the X-ray activity index.

We studied the X-ray activities for different stellar types, by using a well-selected but incomplete sample.

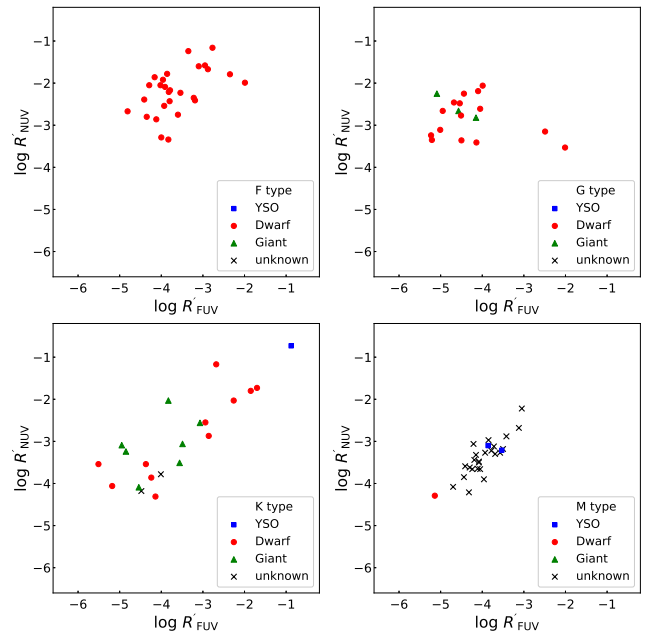


Figure 15. Relation between R'_{NUV} and R'_{FUV} for stars of different spectral types.

The L_X of late-type stars ranges from 10^{27} to 10^{32} ergs s^{-1} . For each stellar type, giants are much brighter than dwarfs and YSOs, while YSOs have higher R_X values than giants and dwarfs. In addition, many giants have very high hardness ratio $HR1$, indicating a high coronal temperature. The L_X and R_X are positively correlated with $HR1$.

This catalog can be used to explore some interesting scientific topics. The activity-rotation relation provides fundamental information on stellar dynamos and angular momentum evolution. With a selected sample, we found that the YSOs, dwarfs, and giants follow a single sequence in the relation R_X versus Ro , while the giants do not follow the relation R_X versus $P_{\text{rot}}^{-2}R^{-4}$ for dwarfs. More stars with period estimations are needed to review these relations. In the future, the TESS mission will cover most of the *Chandra* fields. Combining

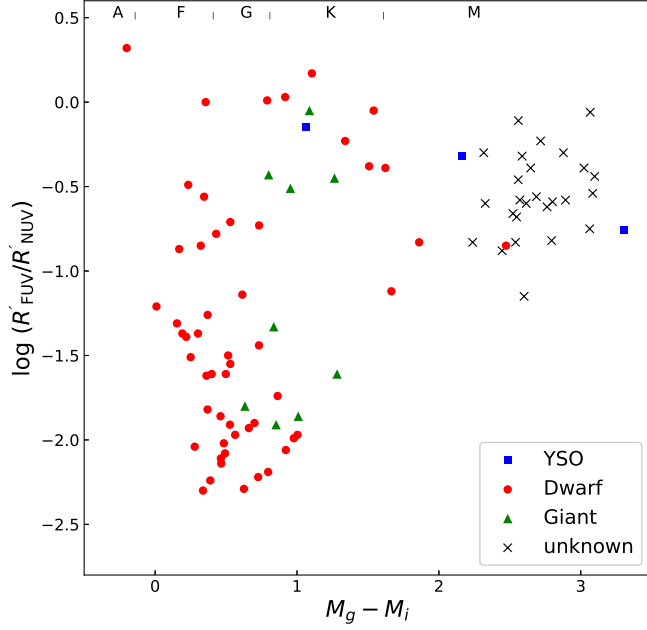


Figure 16. Ratio of FUV and NUV activities as a function of color $M_g - M_i$.

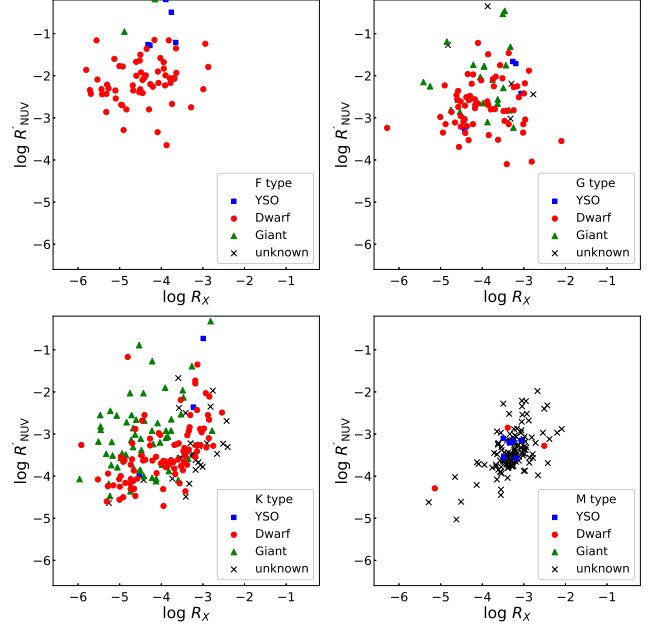


Figure 18. Relation between R'_{NUV} and R_X stars of different spectral types.

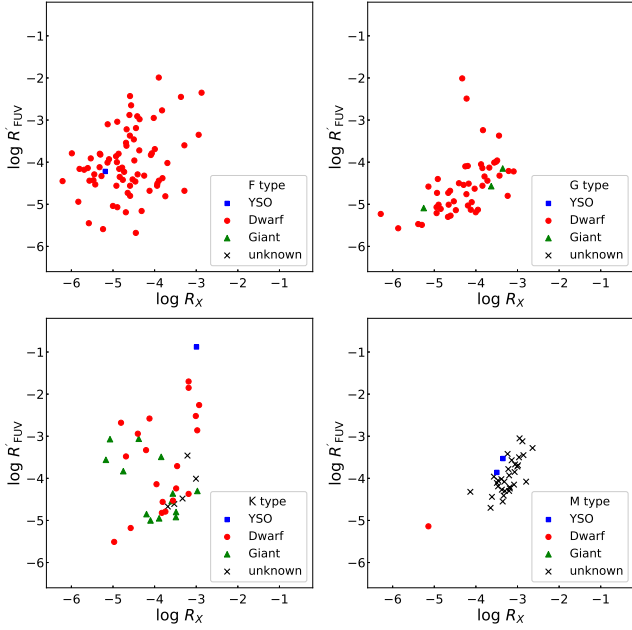


Figure 17. Relation between R'_{FUV} and R_X for stars of different spectral types.

with the rotational periods revealed by TESS, this catalog can help to understand how the magnetic fields and potential dynamo depend on their rotation.

Stars with unexpected high activities are worthy of follow-up detailed studies. A-type stars were expected to have weak large-scale magnetic fields due to their shallow convective envelopes. However, many studies have observed activity of normal A stars through chromospheric emission lines (Simon & Landsman 1991, 1997; Simon et al. 2002) and photospheric stellar spots and flares (Balona 2012, 2013, 2017). Our work shows that

Table 4
Stars with UV emission in our sample.

Object	$\log f_{\text{FUV,exc}}$ (erg cm^{-2} s^{-1})	$\log f_{\text{NUV,exc}}$ (erg cm^{-2} s^{-1})	$\log R'_{\text{FUV}}$	$\log R'_{\text{NUV}}$
(1)	(2)	(3)	(4)	(5)
J000136.1+130639	6.12 ± 0.73	8.25 ± 0.07	-4.81 ± 0.73	-2.67 ± 0.07
J000238.8+255219	...	7.03 ± 0.96	...	-3.47 ± 0.96
J000833.8+512412	8.81 ± 0.04	...	-2.66 ± 0.04	...
J000835.3+512142	7.62 ± 0.08	9.13 ± 0.01	-2.68 ± 0.08	-1.17 ± 0.01
J001325.4+791537	6.60 ± 0.16	8.14 ± 0.05	-4.35 ± 0.16	-2.80 ± 0.05
J001507.9-302342	...	8.34 ± 0.44	...	-2.44 ± 0.44
J001801.8+300816	...	7.77 ± 0.05	...	-2.86 ± 0.05
J001944.6+591349	...	10.71 ± 0.38	...	-0.49 ± 0.38
J002023.5+591444	...	8.54 ± 0.05	...	-2.43 ± 0.05
J002101.6+591518	...	8.40 ± 0.41	...	-2.03 ± 0.41
J002111.3-084140	6.53 ± 0.06	6.98 ± 0.03	-3.12 ± 0.06	-2.68 ± 0.03
J002344.4+641111	...	10.90 ± 0.28	...	-0.19 ± 0.28
J002410.3-020127	...	6.26 ± 0.49	...	-3.95 ± 0.49
J002438.4+641122	...	12.04 ± 0.02	...	-0.05 ± 0.02
J002519.7-123303	5.83 ± 0.47	6.66 ± 0.14	-4.37 ± 0.47	-3.54 ± 0.14
J002537.0-121450	...	6.02 ± 0.35	...	-4.31 ± 0.35
J002609.9+171559	...	6.19 ± 0.24	...	-3.93 ± 0.24
J002611.2+171234	5.54 ± 0.29	...	-5.09 ± 0.29	...
J002756.6+261651	...	7.56 ± 0.11	...	-3.07 ± 0.11
J003151.5+003233	6.02 ± 0.23	6.41 ± 0.13	-3.69 ± 0.23	-3.30 ± 0.13

(This table is available in its entirety in machine-readable and Virtual Observatory (VO) forms in the online journal. A portion is shown here for guidance regarding its form and content.)

many A stars have clear X-ray activity, with $\log R_X$ ranging from ≈ -6 to ≈ -3.5 . Ordinary late-type giants are thought to harbor mainly weak surface magnetic fields, and thus weak stellar activity, due to their large radii and slow rotation. In our sample, more than 700 giants show X-ray emission, and some have high X-ray activity ($\log R_X \approx -3$) and high HR values. This raises the question that whether the solar-like dynamo operates in these stars. Some studies proposed that the X-ray emission of A-type stars and giants are from an unresolved low-mass companion. We are carrying out a campaign of high-resolution spectral observations of some candidates, in order to confirm whether there is a cool companion.

We sincerely thank the anonymous referee for the very helpful constructive comments and suggestions, which have significantly improved this article. We thank Dr. Yang H. Q. and Cui K. M. for developing the *Kepler Data Integration Platform*. This work has made use of data obtained from the *Chandra* Data Archive, and software provided by the *Chandra* X-ray Center (CXC) in the application packages CIAO. This work presents results from the European Space Agency (ESA) space mission *Gaia*. *Gaia* data are being processed by the *Gaia* Data Processing and Analysis Consortium (DPAC). Funding for the DPAC is provided by national institutions, in particular the institutions participating in the *Gaia* MultiLateral Agreement (MLA). This publication makes use of data products from the Pan-STARRS1 Surveys (PS1) and the PS1 public science archive, the Two Micron All Sky Survey, and the Wide-field Infrared Survey Explorer. We acknowledge use of the SIMBAD database and the VizieR catalogue access tool, operated at CDS, Strasbourg, France, and of Astropy, a community-developed core Python package for Astronomy (Astropy Collaboration, 2013). This work was supported by the National Key Research and Development Program of China (NKRDP) under grant numbers 2019YFA0405000, 2019YFA0405504, and 2016YFA0400804, and the B-type Strategic Priority Program of the Chinese Academy of Sciences under grant number XDB41000000. It was also supported by the National Science Foundation of China (NSFC) under grant numbers 11988101 and 11425313.

APPENDIX A
SOFT EXCESS OF A FEW SOURCES

There are about 450 detections with $HR1$ values lower than -0.5 . About 60 detections have vignetting-corrected net counts lower than 10; about 300 detections have counts between 20 and 50; about 90 detections have counts ranging from 50 to 650.

The low HR values are mostly caused by statistical fluctuation of the photons. We also found some sources, with the most counts, show a soft excess in their spectra. This low-temperature thermal component can also help reduce $HR1$ values. Figure 19 shows that the spectra of two sources (J125304.2-091339 and J124836.4-055333) can be best fitted with a two-component model (Black-body plus APEC).

APPENDIX B
YSO CLASSIFICATION

By cross-matching our sample with LAMOST DR7 catalog and Anders et al. (2019), 685 stars in our sample are classified as giants and 3312 ones are dwarfs and YSOs (see Section 2.3). For the remaining sources without classification (“*non-parameter*” sample), many stars with infra-red (IR) excess can be YSO candidates (Figure 20).

We cross-matched our sample with the catalogs in Marton et al. (2016, 2019). There are 1100 objects in common between our sample and these catalogs, including 68 giants, 900 YSOs, and 132 dwarfs. Using these sources, we found that there is no dwarf or giant with color $J - H > 1 - (H - K_S)$ (left panel in Figure 21), while there are only two dwarfs and one giant showing color $W1 - W2 > 0.04$ (right panel in Figure 21). Thus, we will use these two colors as one criterion of classifying YSOs. In addition, as Marton et al. (2019) reported, 99% of the known YSOs are located in the regions where the dust opacity value is higher than 1.3×10^{-5} . Therefore we picked out YSO candidates if one star meets the requirements: (1) $\tau > 1.3 \times 10^{-5}$ and (2) $J - H > 1 - (H - K_S)$ or $W1 - W2 > 0.04$.

However, many AGB stars have color $W2 - W3 < 1$ (Koenig & Leisawitz 2014). For the “*non-parameter*” sample, in which the giants can not be recognized, we add one criterion $W2 - W3 \geq 1$ to select new YSOs.

Finally, with the constraints of colors and dust opacity, we classified additional ≈ 300 stars to be YSOs. We totally determined stellar classes for 3005 sources, including 1196 YSOs, 1112 dwarfs, and 697 giants (Figure 22).

APPENDIX C
BOLOMETRIC LUMINOSITY

We used the PARSEC theoretical models to determine the bolometric luminosity. The PARSEC isochrones¹⁵ were downloaded in eight metallicities ($Z = 0.0001, 0.0005, 0.001, 0.0021, 0.0043, 0.0085, 0.017, 0.034$), with stellar ages $\log(t/\text{yr})$ ranging from 6.6 to 10.13 at steps of $\Delta \log(t/\text{yr}) = 0.02$. We divided our sample into four subsamples: (1) 2872 sources with both parameter estimations and stellar classifications; (2) 1125 sources with parameter estimations but no classification; (3) 1549 sources with classifications but no parameter estimation; (4) 360 sources with neither parameter estimation nor classification.

For subsamples (1) and (2), we first selected the models with closest metallicity, and then extracted the best model by comparing the observed and theoretical T_{eff} and $\log g$ values. Because the PARSEC models divide stars into different evolution stages (e.g., pre-main sequence, main sequence, subgiant, red giant), the models in the same stellar stage were used for the fitting for subsample (1).

For subsamples (3) and (4), we constructed their SEDs ($g, r, i, J, H,$ and K magnitudes) and compared them with the PARSEC models. We used a χ^2 minimization test to determine which PARSEC models are most compatible with the observed SEDs, following

$$\chi^2 = \sum_{i=1}^n \frac{[m_i^{\text{abs}} - m_i^{\text{mod}}(Z, t)]^2}{\sigma_i^2}, \quad (6)$$

¹⁵ <http://stev.oapd.inaf.it/cgi-bin/cmd3.1>

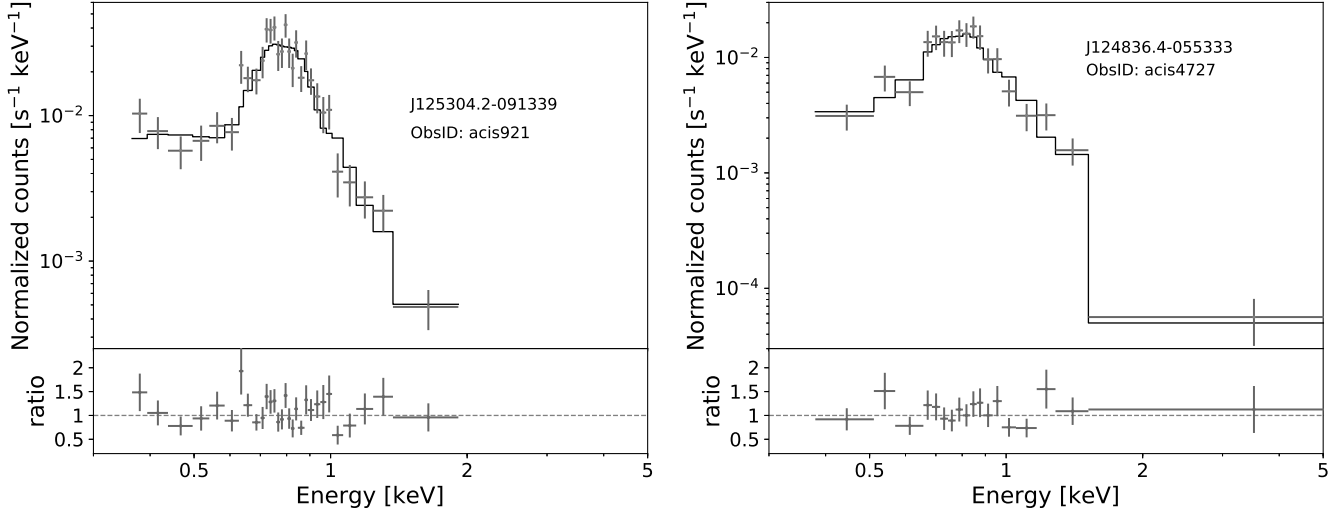


Figure 19. Left panel: best-fit model (Blackbody plus APEC; $kT_{bb} < kT_{apec}$) for J125304.2-091339. Data points and model values are plotted in the top subpanel; data/model ratios in the bottom subpanel. Right panel: best-fit model (Blackbody plus APEC; $kT_{bb} < kT_{apec}$) for J124836.4-055333.

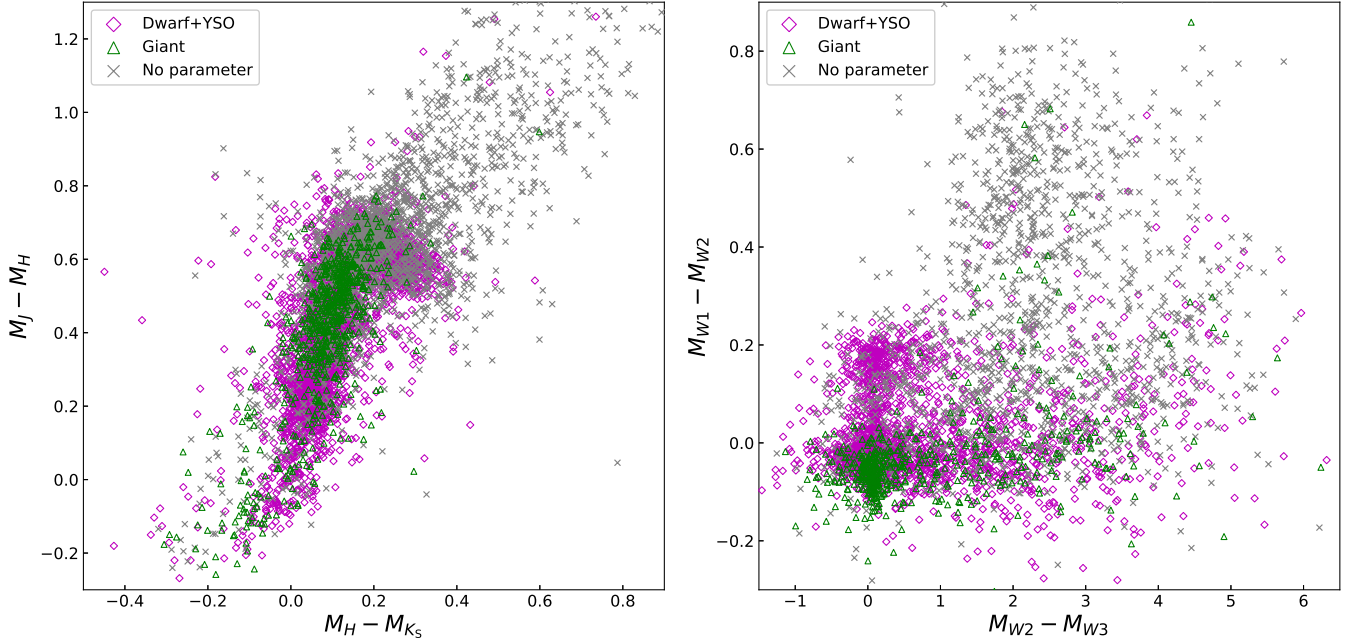


Figure 20. Extinction corrected color-color diagram. The stellar classification is from LAMOST DR7 catalog and Anders et al. (2019), both of which do not separate the main-sequence dwarfs and YSOs. Other objects marked with crosses are from the “non-parameter” sample.

where $m_i^{\text{mod}}(Z, t)$ is the magnitude in the i th filter of a model at metallicity Z and age t , m_i^{abs} represents the absolute observed magnitude in the same filter, σ_i is the observational uncertainty for the i th filter, and n is the number of the filters used for fitting. For subsample (3), we only used the models in the same stellar stage.

REFERENCES

- Anders, F., Khalatyan, A., Chiappini, C., et al. 2019, *A&A*, 628, A94
- Argiroffi, C., Caramazza, M., Micela, G., et al. 2016, *A&A*, 589, A113
- Aurière, M., Konstantinova-Antova, R., Charbonnel, C., et al. 2015, *A&A*, 574, A90
- Ayres, T. R. 2014, *AJ*, 147, 59
- Bai, Y., Liu, J., Wicker, J., et al. 2018, *ApJS*, 235, 16
- Bai, Y., Liu, J., Wang, S., & Yang, F. 2019, *AJ*, 157, 9
- Bailer-Jones, C. A. L., Rybizki, J., Foesneau, M., Mantelet, G., & Andrae, R. 2018, *AJ*, 156, 58
- Balona, L. A. 2012, *MNRAS*, 423, 3420-3429
- Balona, L. A. 2013, *Progress in Physics of the Sun and Stars: A New Era in Helio- and Asteroseismology*, 479, 385
- Balona, L. A. 2017, *MNRAS*, 467, 1830-1837
- Balona, L. A. 2015, *MNRAS*, 447, 2714-2725
- Barnes, S. A. 2003, *ApJ*, 586, 464-479
- Barnes, S. A. 2007, *ApJ*, 669, 1167-1189
- Barnes, S. A. 2010, *ApJ*, 722, 222-234
- Berdyugina, S. V., Berdyugin, A. V., Ilyin, I., & Tuominen, I. 1998, *A&A*, 340, 437-446
- Bianchi, L. 2011, *Ap&SS*, 335, 51-60

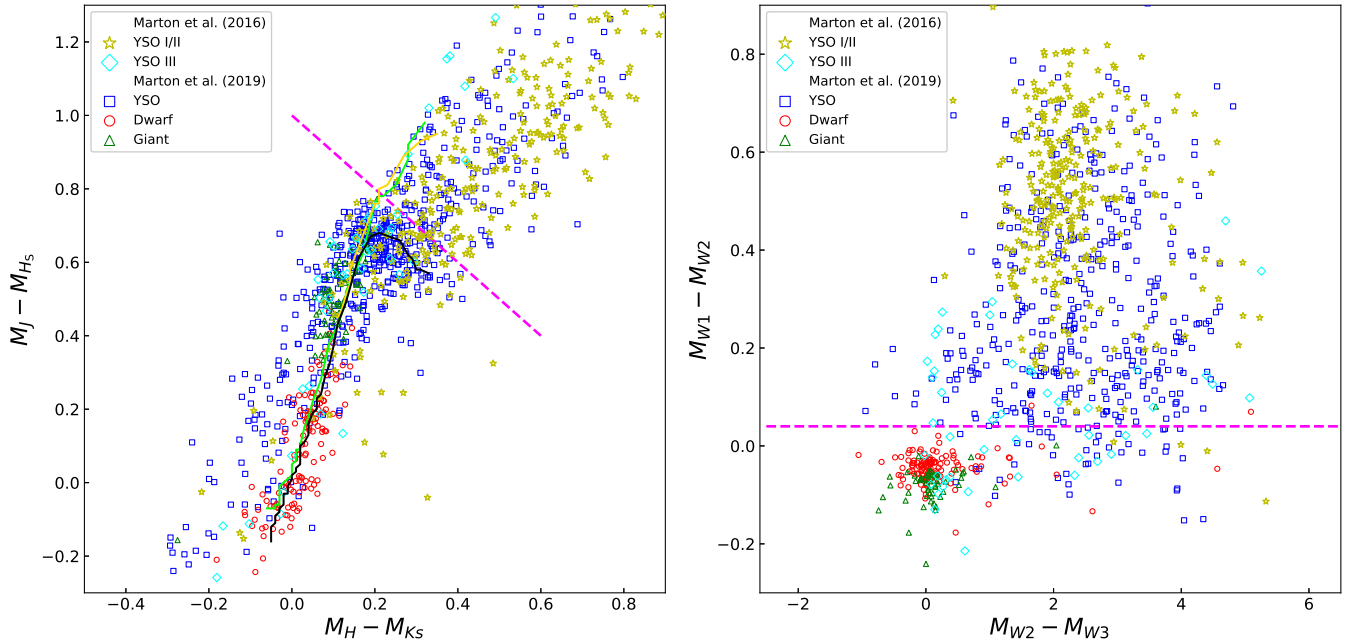


Figure 21. Extinction corrected color-color diagram. The stellar classification is from the catalogs in Marton et al. (2016, 2019). The black, yellow, green lines show the colors of main-sequence stars, giants, and supergiants, respectively (Koornneef 1983). The magenta dashed lines indicate $J - H = 1 - (H - K_S)$ (left panel) and $W1 - W2 = 0.04$ (right panel).

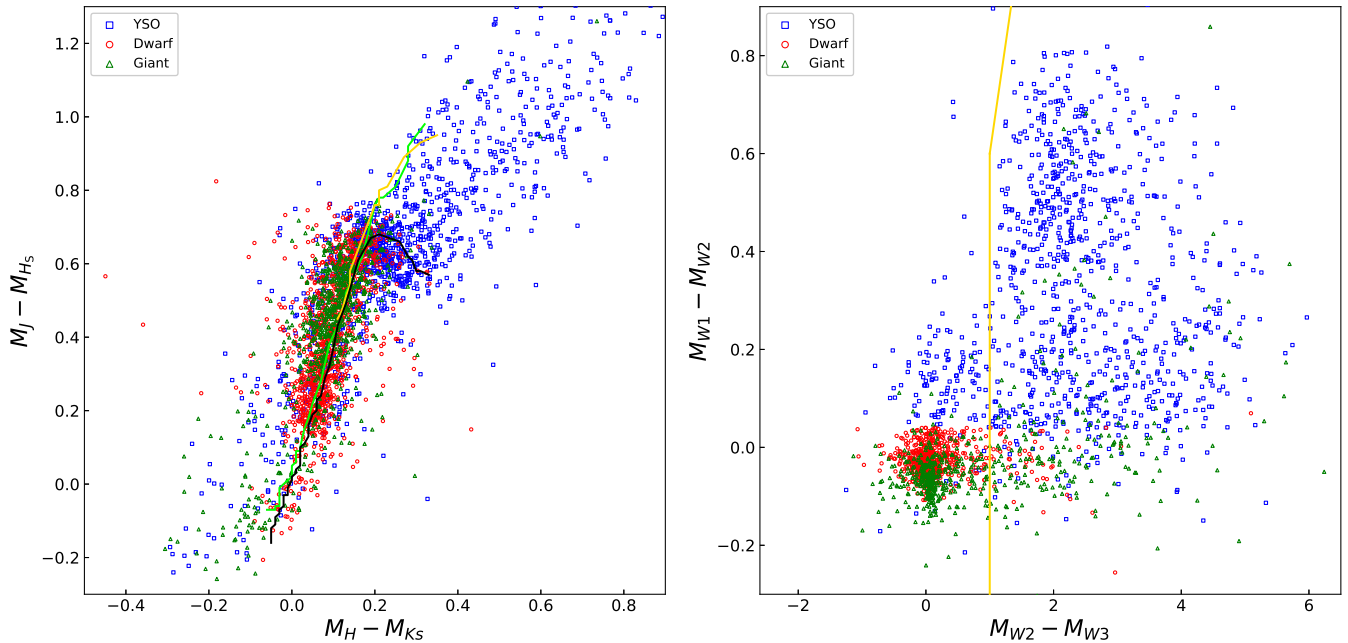


Figure 22. Extinction corrected color-color diagram. Final stellar classification of 3005 sources, including 1196 YSOs, 1112 dwarfs, and 697 giants. The black, yellow, green lines show the colors of main-sequence stars, giants, and supergiants, respectively (Koornneef 1983).

Bilicki, M., Jarrett, T. H., Peacock, J. A., et al. 2014, *ApJS*, 210, 9
 Brun, A. S., García, R. A., Houdek, G., et al. 2015, *Space Sci. Rev.*, 196, 303
 Cardelli, J. A., Clayton, G. C., & Mathis, J. S. 1989, *ApJ*, 345, 245
 Cardini, D., & Cassatella, A. 2007, *ApJ*, 666, 393
 Chambers, K. C., Magnier, E. A., Metcalfe, N., et al. 2016, arXiv e-prints, arXiv:1612.05560
 Ciardi, D. R., von Braun, K., Bryden, G., et al. 2011, *AJ*, 141, 108

Cui, X.-Q., Zhao, Y.-H., Chu, Y.-Q., et al. 2012, *Research in Astronomy and Astrophysics*, 12, 1197
 Cutri, R. M., et al. 2012, *VizieR Online Data Catalog*, II/311
 Feigelson, E. D., Broos, P., Gaffney, J. A., et al. 2002, *ApJ*, 574, 258
 Ferreira Lopes, C. E., Leão, I. C., de Freitas, D. B., et al. 2015, *A&A*, 583, A134
 Flaccomio, E., Micela, G., & Sciortino, S. 2006, *A&A*, 455, 903
 Gaia Collaboration, Babusiaux, C., van Leeuwen, F., et al. 2018, *A&A*, 616, A10

- Gaia Collaboration, Brown, A. G. A., Vallenari, A., et al. 2018, *A&A*, 616, A1
- Gao, Q., Xin, Y., Liu, J.-F., et al. 2016, *ApJS*, 224, 37
- Gilman, P. A. 1983, *ApJS*, 53, 243
- Green, G. M., Schlafly, E. F., Finkbeiner, D. P., et al. 2015, *ApJ*, 810, 25
- Guarcello, M. G., Flaccomio, E., Micela, G., et al. 2017, *A&A*, 602, A10
- Güdel, M. 2004, *A&A Rev.*, 12, 71-237
- Hawley, S. L., Davenport, J. R. A., Kowalski, A. F., et al. 2014, *ApJ*, 797, 121
- He, L., Wang, S., Liu, J., et al. 2019b, *ApJ*, 871, 193
- Hudson, H. S. 1991, *Sol. Phys.*, 133, 357
- Huenemoerder, D. P., Testa, P., & Buzasi, D. L. 2006, *ApJ*, 650, 1119
- Hussain, G. A. J., Jardine, M., Donati, J.-F., et al. 2007, *MNRAS*, 377, 1488-1502
- Jackson, R. J., & Jeffries, R. D. 2010, *MNRAS*, 407, 465
- Jardine, M., & Unruh, Y. C. 1999, *A&A*, 346, 883
- Klimchuk, J. A. 2006, *Sol. Phys.*, 234, 41-77
- Koenig, X. P. & Leisawitz, D. T. 2014, *ApJ*, 791, 131
- Koornneef, J. 1983, *A&A*, 500, 247
- Krakowski, T., Malek, Y. C., Bilicki, M., et al. 2016, *A&A*, 596, A39
- Lehtinen, J. J., Spada, F., Kämpylä, M. J., et al. 2020, *Nature Astronomy*, 4, 658-662
- Lucy, L. B., & White, R. L. 1980, *ApJ*, 241, 300-305
- Luri, X., Brown, A. G. A., Sarro, L. M., et al. 2018, *A&A*, 616, A9
- Maehara, H., Shibayama, T., Notsu, S., et al. 2012, *Nature*, 485, 478-481
- Mamajek, E. E., & Hillenbrand, L. A. 2008, *ApJ*, 687, 1264-1293
- Marino, A., Micela, G., Peres, G., & Sciortino, S. 2003, *A&A*, 407, L63-L66
- Marsden, S. C., Carter, B. D., & Donati, J.-F. 2009, *MNRAS*, 399, 888
- Marton, G., Ábrahám, P., Szegedi-Elek, E., et al. 2019, *MNRAS*, 487, 2522
- Marton, G., Tóth, L. V., Paladini, R., et al. 2016, *MNRAS*, 458, 3479
- Mathur, S., García, R. A., Ballot, J., et al. 2014, *A&A*, 562, A124
- McQuillan, A., Mazeh, T., & Aigrain, S. 2014, *ApJS*, 211, 24
- Meibom, S., Barnes, S. A., Platais, I., et al. 2015, *Nature*, 517, 589
- Namekata, K., Sakaue, T., Watanabe, K., et al. 2017, *ApJ*, 851, 91
- Neilsen, J., Nowak, M. A., Gammie, C., et al. 2013, *ApJ*, 774, 42
- Noyes, R. W., Hartmann, L. W., Baliunas, S. L., Duncan, D. K., & Vaughan, A. H. 1984, *ApJ*, 279, 763-777
- Özdarcan, O., & Dal, H. A. 2018, *Astronomische Nachrichten*, 339, 277-287
- Pace, G. 2013, *A&A*, 551, L8
- Pallavicini, R., Golub, L., Rosner, R., et al. 1981, *ApJ*, 248, 279-290
- Parker, E. N. 1975, *ApJ*, 198, 205-209
- Parker, E. N. 1988, *ApJ*, 330, 474
- Parkin, E. R., Pittard, J. M., Hoare, M. G., Wright, N. J., & Drake, J. J. 2009, *MNRAS*, 400, 629
- Pedersen, M. G., Antoci, V., Korhonen, H., et al. 2017, *MNRAS*, 466, 3060-3076
- Peres, G., Orlando, S., Reale, F., et al. 1997, *Sol. Phys.*, 172, 239
- Peres, G., Orlando, S., Reale, F., et al. 2000, *ApJ*, 528, 537
- Pizzolato, N., Maggio, A., Micela, G., Sciortino, S., & Ventura, P. 2003, *A&A*, 397, 147-157
- Ponti, G., De Marco, B., Morris, M. R., et al. 2015, *MNRAS*, 454, 1525
- Preibisch, T., Kim, Y.-C., Favata, F., et al. 2005, *ApJS*, 160, 401-422
- Prestwich, A. H., Irwin, J. A., Kilgard, R. E., et al. 2003, *ApJ*, 595, 719-726
- Priest, E. R., Heyvaerts, J. F., & Title, A. M. 2002, *ApJ*, 576, 533-551
- Prosser, C. F., Randich, S., Stauffer, J. R., Schmitt, J. H. M. M., & Simon, T. 1996, *AJ*, 112, 1570
- Reid, I. N., & Hawley, S. L. 2000, *New Light on Dark Stars* (New York:Springer)
- Reinhold, T., & Gizon, L. 2015, *A&A*, 583, A65
- Reiners, A., Basri, G., & Browning, M. 2009, *ApJ*, 692, 538
- Reiners, A., Schüssler, M., & Passegger, V. M. 2014, *ApJ*, 794, 144
- Richey-Yowell, T., Shkolnik, E. L., Schneider, A. C., et al. 2019, *ApJ*, 872, 17
- Rosner, R. 1980, *SAO Special Report*, 389, 79
- Rosner, R., Golub, L., & Vaiana, G. S. 1985, *ARA&A*, 23, 413-452
- Sanz-Forcada, J., Stelzer, B., & Metcalfe, T. S. 2013, *A&A*, 553, L6
- Scargle, J. D., Norris, J. P., Jackson, B., et al. 2013, *ApJ*, 764, 167
- Schmitt, J. H. M. M., Golub, L., Harnden, F. R., et al. 1985, *ApJ*, 290, 307-320
- Schmitt, J. H. M. M., Fleming, T. A., & Giampapa, M. S. 1995, *ApJ*, 450, 392
- Shibayama, T., Maehara, H., Notsu, S., et al. 2013, *ApJS*, 209, 5
- Simon, T., Ayres, T. R., Redfield, S., & Linsky, J. L. 2002, *ApJ*, 579, 800-809
- Simon, T., & Landsman, W. 1991, *ApJ*, 380, 200
- Simon, T., & Landsman, W. B. 1997, *ApJ*, 483, 435-438
- Soderblom, D. R. 2010, *ARA&A*, 48, 581-629
- Solanki, S. K., Motamen, S., & Keppens, R. 1997, *A&A*, 325, 1039
- J. R., Hudon, J. D., & Jones, B. F. 1993, *ApJS*, 85, 315
- Stelzer, B. 2017, *Astronomische Nachrichten*, 338, 195-200
- Stelzer, B., Marino, A., Micela, G., López-Santiago, J., & Liefke, C. 2013, *MNRAS*, 431, 2063-2079
- Stępień, K., Schmitt, J. H. M. M., & Voges, W. 2001, *A&A*, 370, 157
- Stocke, J. T., Morris, S. L., Gioia, I. M., et al. 1991, *ApJS*, 76, 813
- Testa, P., Drake, J. J., & Peres, G. 2004, *ApJ*, 617, 508-530
- Testa, P., Saar, S. H., & Drake, J. J. 2015, *Philosophical Transactions of the Royal Society of London Series A*, 373, 20140259-20140259
- Ustamujic, S., Orlando, S., Bonito, R., Miceli, M., & Gómez de Castro, A. I. 2018, *A&A*, 615, A124
- Vaiana, G. S., Cassinelli, J. P., Fabbiano, G., et al. 1981, *ApJ*, 245, 163-182
- Vaiana, G. S. 1983, *Solar and Stellar Magnetic Fields: Origins and Coronal Effects*, 102, 165-185
- van Ballegoijen, A. A., Asgari-Targhi, M., Cranmer, S. R., & DeLuca, E. E. 2011, *ApJ*, 736, 3
- van Ballegoijen, A. A., Asgari-Targhi, M., & Berger, M. A. 2014, *ApJ*, 787, 87
- van Saders, J. L., & Pinsonneault, M. H. 2013, *ApJ*, 776, 67
- Vilhu, O. 1984, *A&A*, 133, 117-126
- Vilhu, O., & Walter, F. M. 1987, *ApJ*, 321, 958
- Walkowicz, L. M., Basri, G., Batalha, N., et al. 2011, *AJ*, 141, 50
- Wang, S., Liu, J., Qiu, Y., et al. 2016, *ApJS*, 224, 40
- Wolk, S. J., Harnden, F. R., Flaccomio, E., et al. 2005, *ApJS*, 160, 423-449
- Wright, N. J., & Drake, J. J. 2016, *Nature*, 535, 526-528
- Wright, N. J., Drake, J. J., Mamajek, E. E., & Henry, G. W. 2011, *ApJ*, 743, 48
- Yang, H., & Liu, J. 2019, *ApJS*, 241, 29
- Zhao, G., Zhao, Y.-H., Chu, Y.-Q., et al. 2012, *Research in Astronomy and Astrophysics*, 12, 723
- Zacharias, N., Finch, C. T., Girard, T. M., et al. 2013, *AJ*, 145, 44
- Zhu, H., Tian, W., Li, A., & Zhang, M. 2017, *MNRAS*, 471, 3494-3528